PHYSICAL REVIEW ACCELERATORS AND BEAMS **25,** 121002 (2022)

RHIC optics and spin dynamics with snakes and rotators

F. Méot, H. Huang, V. Ptitsyn, V. Ranjbar, G. Robert-Demolaize, and V. Schoefer
Brookhaven National Laboratory, Upton, New York 11973, USA

V. Morozov
Oak Ridge National Laboratory, Oak Ridge, Tennessee 37831, USA

(Received 1 October 2022; accepted 6 December 2022; published 27 December 2022)

The operation of RHIC collider rings in polarized proton runs includes helical snakes, which allow for preserving polarization during acceleration to store energies. The RHIC lattice also includes spin rotators, operated when nonvertical polarization or corrections to the orientation of polarization at the interaction points are required. Utilization of OPERA field maps of snakes and rotators has been systematized in the past decade, in order to assess in detail the effects of these spin devices on beam polarization, and their perturbative effects on beam optics. The method is also used in ongoing studies regarding the future Electron Ion Collider, to permit increasing average store polarization to at least 70% at 275 GeV and the acceleration of polarized helion with low polarization losses. This paper reviews various applications and outcomes of these field map methods. It is thereby also a review of studies undertaken as part of beam polarization research activities at RHIC in recent years.

DOI: 10.1103/PhysRevAccelBeams.25.121002

I. INTRODUCTION

The RHIC collider lattice comprises helical snakes, which allow preserving proton beam polarization during acceleration from 23.8 to 100 GeV and 255 GeV store energies [1]. Additional snakes will be included for the future Electron Ion Collider, to allow pushing store energy to 275 GeV and accelerate polarized helion beams [2]. RHIC lattice also includes spin rotators, operated when nonvertical polarization or corrections to the orientation of polarization at the interaction points are required [3].

An overview of the RHIC facility and its polarized proton beam equipments is given in Fig. 1. Snakes in both Blue and Yellow rings are located azimuthally π apart; rotators are located on both sides of IR6 (STAR) and IR8 (Phenix and super-Phenix) interaction regions. Polarimetry includes Carbon target (p-C) polarimeters and a hydrogen jet (H-jet) at IP12, as well as local polarimeters at the detectors.

Details regarding the design, electromechanical, and magnetic parameters of RHIC helical dipoles can be found in dedicated publications [1,3–6]. From the early times of the design and production stages of RHIC snakes and rotators, TOSCA/OPERA field maps have been produced [7,8], so allowing accurate modeling of the field along the helical trajectories, thereby allowing accurate computation of spin motion [8,9]. During the past decade, a systematic approach has been developed to include OPERA field maps as optical elements in modeling the RHIC lattice. This followed earlier work to develop field map based optical elements to represent the two helical partial snakes [10], as well as the combined function main dipoles [11], in the AGS ring lattice model.

In that manner, specific effects of these devices on beam and spin optics can be assessed with great accuracy from their field. This includes orbit defects (field integrals

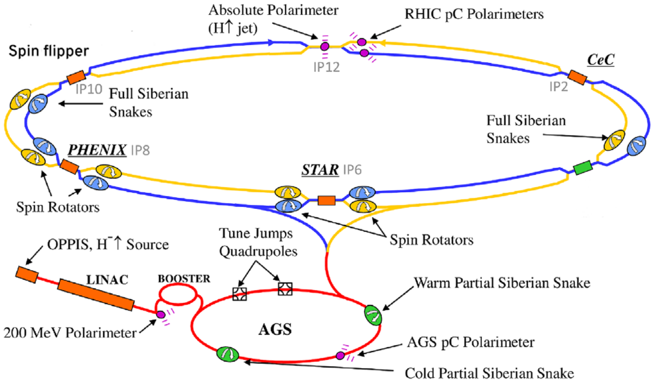

FIG. 1. Schematic layout of RHIC polarized beam complex. RHIC consists of two rings, respectively, known as Blue and Yellow. Beams go clockwise (CW) in the former, and counter-clockwise (CCW) in the latter. Snakes are located at 9 o'clock and 3 o'clock, rotator pairs flank IP6 and IP8.

$\int B_{x,y}\, ds$ do not exactly cancel), tune shift (first order field terms matter as well as feed-down from a large excursion at low energy), coupling, chromaticity, the dependence of spin rotation on beam rigidity, effects of end fringe fields, the impact of local vertical closed orbit bump on spin closed orbit.

Obviously, the full benefit of using field maps to model magnetic fields leans on the numerical solution of the differential equations of particle and spin motion, which is the technique used in the studies discussed here.

Various outcomes of these methods, in different contexts, are addressed in the following sections:

Section II introduces RHIC snakes and their optical and spin properties; in Sec. III, OPERA field maps are used as optical elements proper in the RHIC lattice computer model, outcomes regarding beam and spin optics are discussed; Sec. IV applies the field map method to solving an issue concerning the RHIC Blue 9 o'clock snake, an incident which occurred at the start of RHIC Run 22; Sec. V introduces RHIC rotators; RHIC lattice modeling including the 16 snake and rotator field maps is addressed in Sec. VI; Sec. VII plays with snakes operated in "spin transparency" mode; Sec. VIII concludes this study.

II. RHIC SNAKES

RHIC snakes are comprised of four identical, $\lambda = 2.4$ m long, 360°-twist, right-handed helix dipoles with alternate current signs, represented in Fig. 2 by the following series:

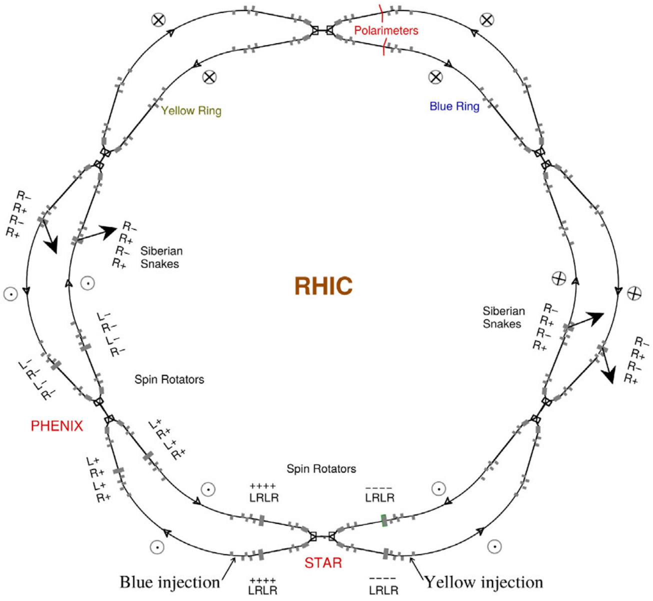

FIG. 2. $R+R-R+R-$ and $R-R+R-R+$ four-helix snakes in RHIC Blue and Yellow rings, at 9 o'clock and 3 o'clock. The beam goes clockwise in Blue, counterclockwise in Yellow.

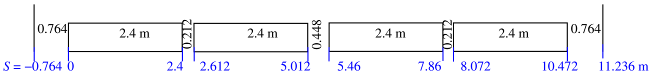

FIG. 3. A sketch of RHIC snake and rotator layouts, each rectangle represents a 2.4 m long 360°-twist helix. Field maps from the OPERA model extend an extra 0.764 m at both ends, to encompass field falloffs.

$$\begin{array}{cc} 9\text{ o'clock, Blue (CW)} & 3\text{ o'clock, Blue (CW)} \\ \text{and} & \text{and} \\ 3\text{ o'clock, Yellow (CCW):} & 3\text{ o'clock, Yellow (CCW):} \\ R+R-R+R- & R-R+R-R+ \\ +100/-322/+322/-100\,\text{A} & -100/+322/-322/+100\,\text{A} \end{array}$$

The four helices are spaced 0.212/0.448/0.212 m hence an overall snake length of 10.472 m (Fig. 3). The magnetic field is oriented vertically at snake ends. to the longitudinal axis.

A 12-m extent OPERA model of a complete snake (Fig. 4), computed for nominal helix currents, is available; it has been shown that a string of independent field maps of each of the four helices can be used equivalently, with the same outcomes [12]. So far as RHIC lattice modeling is concerned, the latter method is preferred: each 360°-twist helix has its independent field map, as this allows simulating actual operation conditions such as addressed in Sec. III where the two outer helices (respectively the two inner helices) are powered in series; it further allows simulating independent current setting in each helix. Additionally, a left-handed helix map can be created from a right-handed one—no need for specific OPERA computation—as discussed in Sec. V, so providing the left-handed elements necessary to simulate RHIC rotators.

Two helix OPERA field maps are available, for, respectively, the outer and inner helix: in normal "full snake" operation, a snake outer helix field is about 1.3 T, and its

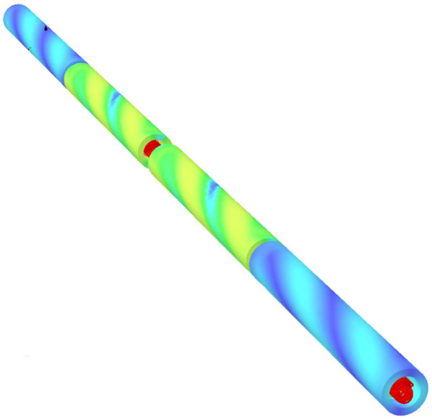

FIG. 4. OPERA model of RHIC four-helix snakes and rotators.

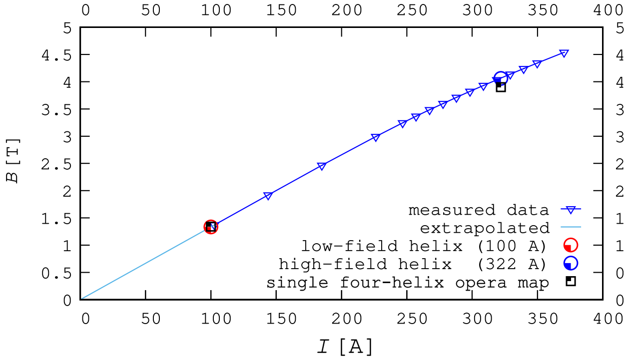

FIG. 5. Numerical data used for the normalization of OPERA currents to real-life currents. Blue triangles: from field measurements in a prototype 360°-twist helical dipole. Red circle: low-field helix map, case of 100 A OPERA current; Blue circle: high field helix map, case of 322 A OPERA current. Black squares: a case of a 12 m extent OPERA model of a complete snake computed with $(I_{\mathrm{out}}, I_{\mathrm{in}}) = (100, 322\ \mathrm{A})$ [12].

field map has been computed at low field ($I_{\mathrm{out}} = 100$ A current); an inner helix field is about 4 T, its field map has been computed at high field ($I_{\mathrm{in}} = 322$ A current).

Field normalization—Magnetic field measurements have established the correspondence from feed current to maximum field amplitude along the 360°-helix axis, in the case of a single helix. This allows to account for field saturation as the current increases, so giving a correspondence between OPERA and real-life currents. The data of concern are displayed in Fig. 5, which includes the case of a low-field helix OPERA map (computed with 100 A), a high-field helix OPERA map (computed with 322 A), as well as the case of a single four-helix field map computed with $(I_{\mathrm{out}}, I_{\mathrm{in}}) = (100, 322\,\mathrm{A})$.

Field normalization is relevant when moving to required currents for the rotator operation of the helices (Sec. V), and for the spin transparency operational mode of the snakes (Sec. VII): in both cases, helix currents I_{out} and I_{in} differ in a substantial manner from the "full snake" 100 A/322 A setting.

Note that, although $B(I)$ measurements (the blue triangles in Fig. 5) used a stand-alone helix, a four-helix single-map OPERA computation (the two square markers) yields a slightly lower field in the high-field helix for the same current, 322 A. These differences in field values are marginal anyway: at 100 and 322 A, the measured low and high field in the magnet prototype is, respectively, 1.337 and 4.066 T, whereas for these very current values, OPERA yields, respectively, either 1.340 and 3.903 T in the case of the four-helix full-snake or 1.336 and 4.068 T, single helix case. These small differences have a negligible effect on spin rotation; details can be found in Ref. [12].

Theoretical expectations—In this document, a (x, s, y) Serret-Frénet frame is used (radial, longitudinal, vertical); in both Blue and Yellow rings, the longitudinal axis is oriented in the beam direction, CW in Blue, CCW in Yellow, and the radial axis points outward (curvature is negative, dispersion is positive). An index "l" is used for the longitudinal vector component in the following. Helix parameters at injection and store energies, obtained from either transport through the OPERA field map or from theory, are compared in Table I. In particular, the spin rotation angle expresses as

$$\mu = 2\pi\sqrt{1+\chi^2} \quad \text{with} \quad 2\pi\chi = (1+G\gamma)\frac{B_0\lambda}{B\rho} \tag{1}$$

(λ is the helix length and pitch; B_0 is its field [Eq. (3)]; G is the gyromagnetic anomaly, $G = 1.7928$ for protons; $\gamma =$ Lorentz relativistic factor), and the rotation axis (with $\epsilon = \pm 1$ for, respectively, right or left helicity) writes

$$(\mathrm{rad}, \mathrm{long}, \mathrm{vert}):\ \left(0, \frac{-\epsilon}{\sqrt{1+\chi^2}}, \frac{-\epsilon\chi}{\sqrt{1+\chi^2}}\right) \tag{2}$$

(the radial, longitudinal and vertical components of the precession axis are quoted in parentheses). The rotation axis lies in the (s, y) vertical plane at an angle $atan(1/\chi)$ to the y axis. Perturbations in snake angle settings amounting to such slight differences as observed in Table I between theoretical and field map data may result in substantial changes in spin closed orbit $\vec{n}_0(s)$ around the ring, including perturbation of $\vec{n}_0$ orientation at collision points, and in the departure of spin tune from ½, this will be addressed in next sections.

The theoretical field across a 360°-twist helix is, to the second order in the transverse coordinates [1, Eqs. 4.1-3],

$$\begin{cases} B_x/B_0 = -\sin(ks)[1+\frac{k^2}{8}(3x^2+y^2)] + \frac{k^2}{4}xy\cos(ks) \\ B_y/B_0 = \cos(ks)[1+\frac{k^2}{8}(x^2+3y^2)] - \frac{k^2}{4}xy\sin(ks) \\ B_l/B_0 = -k[x\cos(ks) + y\sin(ks)] \end{cases} \tag{3}$$

with s the distance along the helix axis and origin $s = 0$ at the entrance of the helix, and with

TABLE I. Spin rotation (μ), and angle of precession axis to the vertical axis (x-tilt), in low-field ($B_0 = 1.337$ T) and high-field ($B_0 = 4.07$ T) RHIC snake helices, from their OPERA field maps (num.) and from theory (theor.) for comparison.

		Low-field (+100 A)		High-field (+322 A)	
		μ	x-tilt	μ	x-tilt
$G\gamma$		(deg)		(deg)	
45.5	num.	14.95	105.82	120.45	131.29
	theor.	15.77	106.66	126.95	132.33
489	num.	14.93	105.87	120.13	131.28
	theor.	15.15	106.34	122.50	131.75

$$k = \epsilon\frac{2\pi}{\lambda}, \qquad \epsilon = \pm 1 \quad \text{the helicity.} \tag{4}$$

RHIC snake helices are right-handed ($\epsilon = +1$) with alternate field signs; helix pitch $\lambda = 2.4$ m; field at ends is vertical: $\vec{B}(s = 0) = (0, 0, \pm B_0)$ in the hard-edge model. The field along the helical trajectory arc in the OPERA field map of an R + helix is displayed in Fig. 6. Given the radial excursions of concern, namely $|x|, |y| < 2.5$ cm, while $k^2/8 \approx 1$ m^{-2}, nonlinear terms only contribute weakly to the field.

The parametric equations of particle trajectory through a helix are

$$\begin{cases} x(s) = \frac{-B_0}{k^2 B\rho}[1 - \cos(ks)] + x_0 + x_0' s \\ y(s) = \frac{-B_0}{k^2 B\rho}\sin(ks) + y_0 + \left(y_0' + \frac{B_0}{kB\rho}\right)s \end{cases} \tag{5}$$

with (x_0, y_0), (x_0', y_0') are the entrance position and incidence. Assuming null incidence ($x_0' = y_0' = 0$), the trajectory ends up vertically shifted as $x(\lambda) = x_0$ and $y(\lambda) = y_0 + B_0/kB\rho$ so that two successive helices with opposite signs of $B_0 \times \epsilon$ ensure orbit transparency and equal initial and final coordinates.

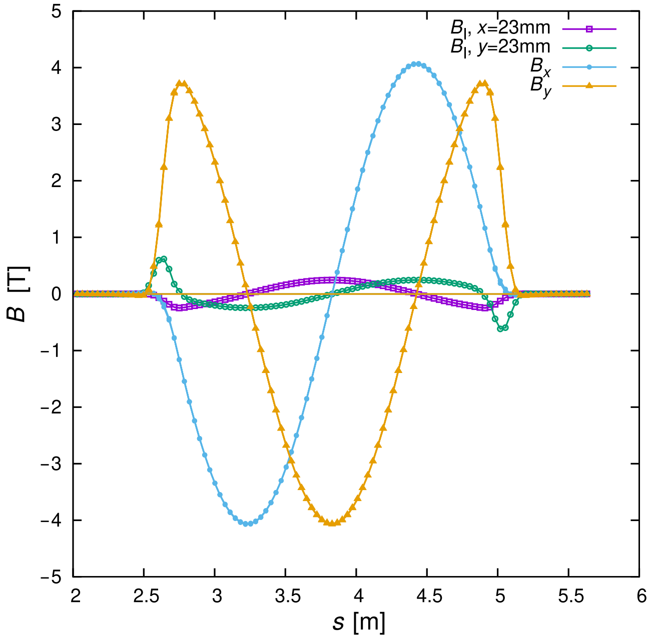

FIG. 6. Field along the helical trajectory arc across a R+ snake helix (using its OPERA field map, current $I_{\rm in} = 322$ A, $B_0 = 4.07$ T positive, $k > 0$). Two cases are displayed: $x_0 = 23$ mm or $y_0 = 23$ mm, all other coordinates are zero: the transverse field components are verified to be essentially independent of $x(s)$ and $y(s)$: $B_x \approx -B_0 \sin(ks)$, $B_y \approx B_0 \cos(ks)$ (Eq. (3), with yet a noticeable effect of field falloffs at helix ends.

It requires at least three 360°-twist helices to constitute a full helical snake [13], whereas a helix pair only allows a partial snake (spin precession < 180°), the latter case is addressed in Sec. IV. Four helices in series, as in RHIC, allow independent control of spin rotation and rotation axis orientation as well as orbit transparency.

Figure 7 displays the transverse projection of particle motion through the RHIC four-helix snake, as obtained from motion integration through their four successive OPERA maps. In RHIC operation, at low energy where the helix excursion is larger and reaching for instance 23 mm at injection, y_0 is adjusted to vertically center the closed orbit along the snake (Fig. 7). The incoming incidence, and thus the outgoing incidence by virtue of Eq. (5), is normally zero, however a vertical incidence $y_0' \neq 0$ may be resorted to for the purpose of geometrical acceptance (see Sec. IV).

At low energy, sextupole feed-down causes a tune shift (Sec. III, see Table II, column 4). Beyond, given the orbit excursion in the RHIC energy range, the effects of nonlinear terms are weak, nevertheless field maps capture these effects, should these effects impact the especially sensitive spin dynamics.

Tracking through an RRRR field map series yields, at all energies in the range of 23–300 GeV, a first order transverse transport matrix close to (with $L \approx$ snake length)

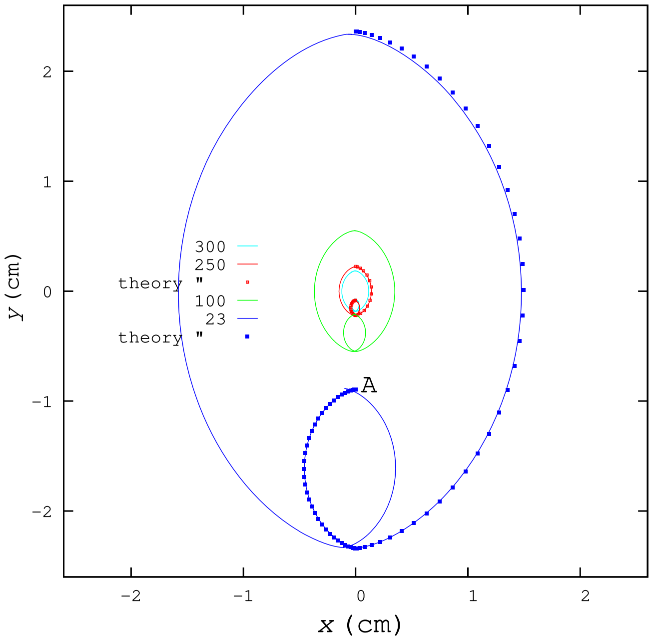

FIG. 7. Transverse projection of the helical motion across an R + R − R + R− snake series, using OPERA field maps. A smaller excursion is in the outer, low-field helices. Solid lines are from motion integration through field maps, at 23 and 100 GeV and, very close to each other, 250 and 300 GeV; markers at 23 and 250 GeV are from theory [Eq. (5)]. RHIC closed orbit goes counterclockwise from the top of a smaller helix, "A" for instance at 23 GeV.

TABLE II. RHIC and spin closed orbit parameters, $G\gamma = 45.5$. Column 1: bare RHIC ring, no field maps, flat orbit; column 2: vertical orbit bumps in snake region are set, no field maps; column 3: the orbit is flat, except over the 10.472 m helical path across snake field maps which are ±0.8 cm offset; column 4: normal polarized proton operation: snake field maps and local vertical closed orbit bumps are in place in the RHIC lattice model.

	Bare RHIC	Orbit bumps set, no maps	Maps offset, no bumps	Maps and orbit bumps
ν_x	28.6973	28.6993	28.6935	28.6918
ν_y	29.6895	29.6887	29.7518	29.7067
ξ_x	2.5	2.0	0.9	0.2
ξ_y	4	2.6	4.5	8.1
$\nu_x - \nu_y$ coupling strength	0	0.007	≈0	0.009
$\vec{n}_0$ vector: see Figure	13	13	14	15
$\vec{n}_0$ tilt	0	0	0	3.5°
Spin tune ν_{sp}	0.4632	0.4659	0.4873	0.4987

$$T_{\mathrm{snake}} \approx \begin{pmatrix} 1 & L & \mathcal{O}(10^{-2}) & -\mathcal{O}(10^{-4}) & 0 \\ 0 & 1 & & & 0 \\ \mathcal{O}(10^{-2}) & -\mathcal{O}(10^{-4}) & 1 & L & 0 \\ & & 0 & 1 & 0 \end{pmatrix}. \tag{6}$$

At higher energies, this matrix approximation becomes more accurate. The dispersive terms (rightmost column of the matrix) are quasi-zero and the transverse coupling terms (anti-diagonal) are small (order of magnitude as indicated, lower at higher energy).

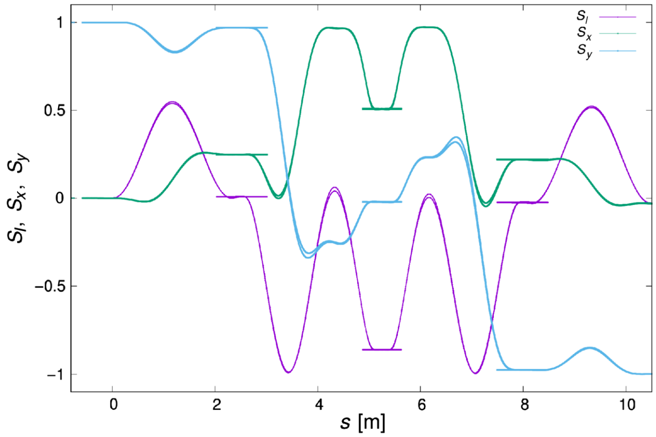

FIG. 8. Evolution of the spin components along the helical trajectories of Fig. 7 (from vertical initial spin), at 23 and 250 GeV. It can be observed that spin motion across the snake is essentially independent of energy, as expected: except for the 3–7 m region where the 23- and 250-GeV S_y components do not fully coincide, the $\vec{S}(s)$ components at both energies essentially superimpose at this scale. The small back-forth segments at helix ends are field map manipulation artifacts.

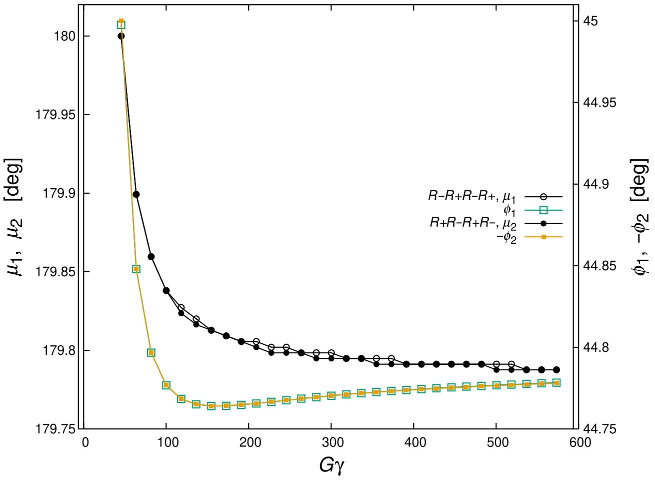

FIG. 9. Energy dependence of $\mathrm{R}-\mathrm{R}+\mathrm{R}-\mathrm{R}+$ (index 1) and $\mathrm{R}+\mathrm{R}-\mathrm{R}+\mathrm{R}-$ (index 2) snake series angles, over [23.8, 300] GeV (the solid lines are to guide the eye). The OPERA model currents for precisely $\mu = 180°$ and $\phi = 45°$ at 23.8 GeV ($G\gamma = 45.5$) are $I_{\mathrm{out}} = 93.35$ A, $I_{\mathrm{in}} = 321.87$ A.

To summarize, T_{snake} matrix outcomes from field maps indicate that perturbation of optical functions and tunes is expected at low energy, whereas the contribution of snakes proper to coupling is expected to be small; this is investigated further in Sec. III. On the other hand, orbit-wise, a snake may be approximated by a drift (as in the case of the RHIC operation MADX model), which does not preclude including the local closed orbit bump necessary for centering the helix as illustrated in Fig. 7.

Spin flip motion along a snake, at 23 and 250 GeV, is displayed in Fig. 8; the graph shows that $S_{x,l,y}(s)$ spin components depend only weakly upon energy, as a result of that very property of $B_{x,y}$ [Eq. (3)]. This is detailed in Fig. 9 which displays the energy dependence of spin rotation angle μ, and spin precession axis orientation ϕ, over the energy range 23–300 GeV, computed using OPERA maps. Tracking delivers a spin rotation matrix

$$R_{\mathrm{sp}} \approx \begin{pmatrix} 0 & \pm 1 & 0 \\ \pm 1 & 0 & 0 \\ 0 & 0 & -1 \end{pmatrix} \tag{7}$$

for, respectively, the $\mathrm{R}-\mathrm{R}+\mathrm{R}-\mathrm{R}+$ and $\mathrm{R}+\mathrm{R}-\mathrm{R}+\mathrm{R}-$ series, which is the expected matrix for a 180° rotation around an axis in the horizontal plane at ±45° from the longitudinal axis.

III. RHIC LATTICE WITH SNAKE FIELD MAPS

A typical RHIC 2022 (Run 22) operational model optics for the Yellow ring is used for the analysis in this section.

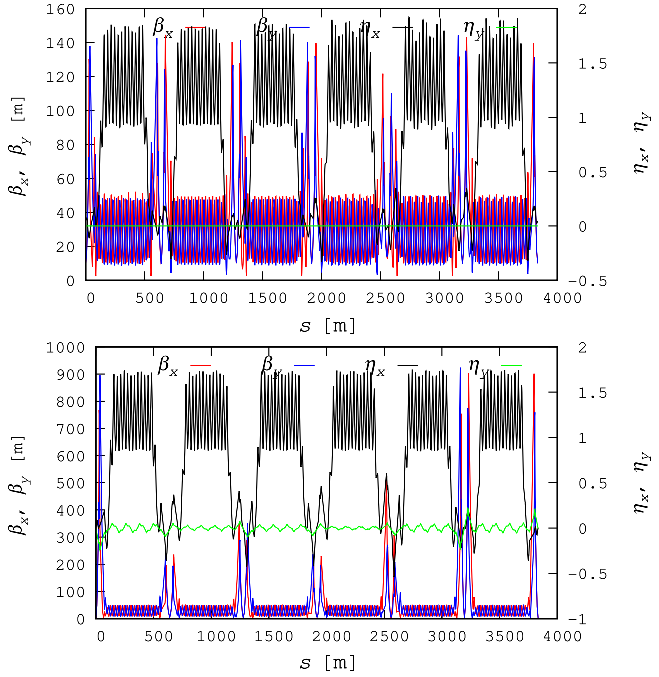

FIG. 10. For reference, optical functions in RHIC Run 22 Yellow lattice injection (top) and 255 GeV (bottom) nominal models, prior to any insertion of snake or rotator OPERA field maps and their local centering bumps. The small vertical dispersion at 255 GeV results from vertical orbit separation bumps at the six interaction points (Sec. III B). Origin of s is at IP6 (STAR detector), s increases going CCW.

For reference in this and subsequent sections, Fig. 10 displays the optical functions and Table III lists the main parameters, in the absence of any snake and rotator field maps.

Referring to Fig. 2, the moving frame has its longitudinal axis (s) in the beam direction (CCW), its radial axis (x) points outward (curvature is negative, dispersion is positive, Fig. 11), and its vertical axis (y) points down.

Regarding the snake OPERA field maps inserted in that lattice in the present section, low field and high field helix currents applied are, respectively, $I_{\text{out}} = 93.35$ A, $I_{\text{in}} = 321.87$ A, so ensuring $(\mu, \phi) \approx (180, \pm 45)$ at a few per mil accuracy, over 23–300 GeV (Fig. 9).

TABLE III. RHIC Yellow lattice without snakes, Run 22 reference parameters, at injection and store energies. The orbit is taken flat at injection and featuring vertical separation bumps (up to 6 mm) at IPs, at 255 GeV.

		23.8 GeV	255 GeV
Orbit length	(m)	3833.845	
ν_x, ν_y		28.697, 29.690	28.691, 29.685
ξ_x, ξ_y		3, 3	
$x_{\text{co}}, y_{\text{co}}$ max.	(mm)	0, 0	0.6, 6
η_x, η_y max.	(m)	1.88, 0	1.74, 0.25
β_x, β_y max.	(m)	144, 143	928, 881

The effect of spin rotators on this Yellow ring Run 22 lattice will be considered in Sec. V.

A. Injection optics

Typical closed orbit and optical functions around the RHIC Yellow ring, obtained using the eight OPERA field maps of 9 o’clock and 3 o’clock snakes, are given in Fig. 11. The local vertical orbit bumps extend over ≈90 m in both snake regions, 3 o’clock and 9 o’clock as shown in Fig. 12, they aim at centering the helical orbit along the snake (as in Fig. 7). Comparison with Fig. 10 shows that the introduction of snakes and their local orbit bumps results in a substantial modulation of the optical functions in the arcs.

Table II and Figs. 13–15 detail basic optical and spin parameters obtained by tracking four different model configurations, namely, bare RHIC ring, no snake field maps, flat orbit (Fig. 13); vertical orbit bumps in snake region set, no field maps (Fig. 13); a second version of the regular MADX RHIC operation model; flat orbit except over the ≈10.5 m helical path across snake field maps; snake currents are set for $\mu = 180°$ and $\phi = \pm 45°$, i.e., $I_{\text{out}} = 93.35$ A, $I_{\text{in}} = 321.87$ A, with appropriate signs; snakes are ±0.8 cm offset so that the helical orbit is centered on the inner helix axis, similarly to the configuration in Fig. 7 (Fig. 14); normal polarized proton

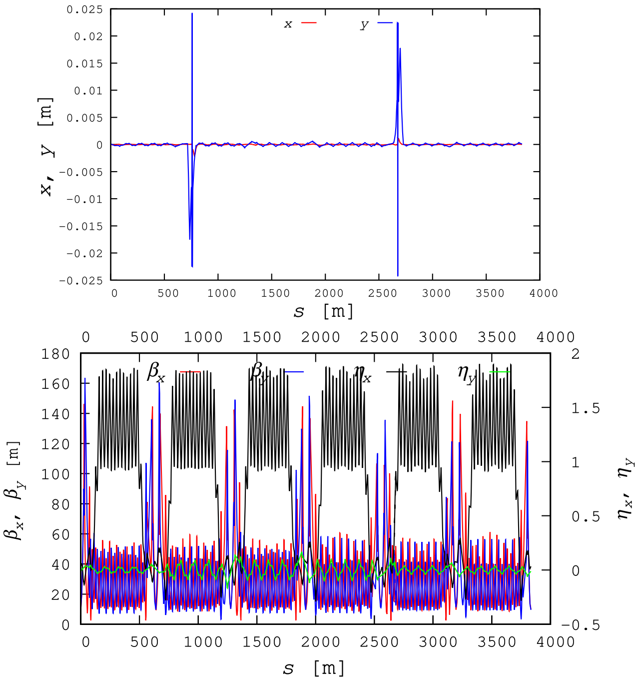

FIG. 11. Closed orbit (top) and optical functions (bottom) in RHIC Yellow ring lattice model at injection energy ($G\gamma = 45.5$), with snake lattice elements represented by their OPERA field maps and including the local centering bumps.

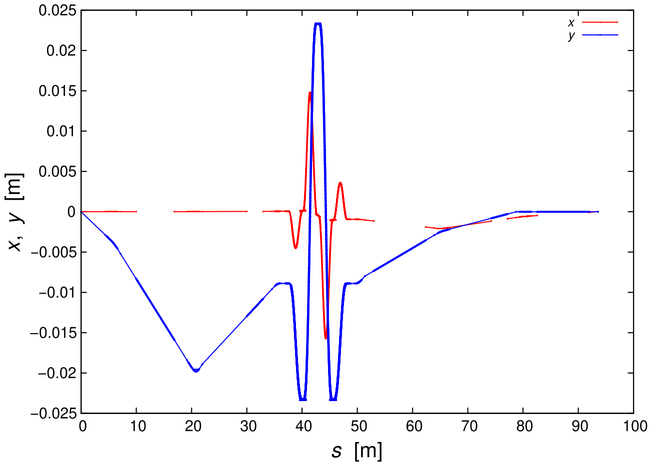

FIG. 12. Local horizontal (red) and vertical (blue) closed orbit bumps in the 3 o’clock snake region of the RHIC ring, using OPERA field maps. The 9 o’clock bump is similar, with reversed signs.

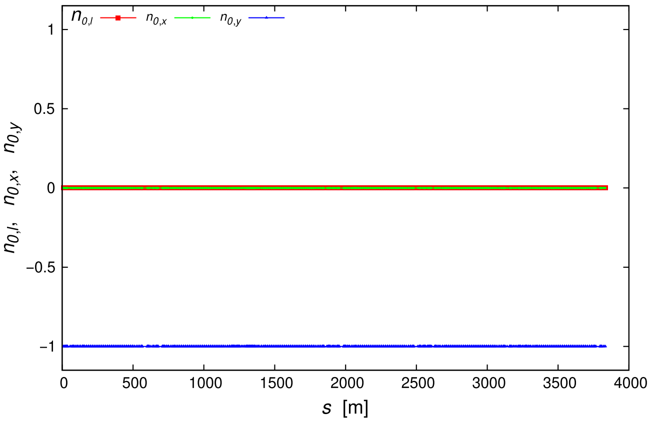

FIG. 13. Spin $\vec{n}_0$ vector around Yellow ring and tilt angle. No snakes, here, $G\gamma = 45.5$. Two trivial cases for reference, both yielding vertical spin closed orbit: on one hand bare, perfect, Yellow ring, flat orbit, and on the other hand, with 90 m extent vertical orbit bumps set in snake regions.

operation: snake field maps and local vertical closed orbit bumps for helix centering are in place (Fig. 15).

These results show that (i) introducing field maps of 3 o’clock and 9 o’clock snakes in the ring lattice has a marginal effect on the horizontal tune and causes a vertical tune shift $\delta\nu_y \approx 0.06$ (Table II, columns 1 and 2), both in accord with tune measurements performed in RHIC; it causes a noticeable perturbation of the optical functions, cf., Figs. 10 and 11; (ii) snake field maps only introduce negligible coupling (Table II, column 3): $\int B_l(r)\,ds$ along a 360°-twisted dipole is about zero [Eq. (3), Fig. 6] confirmed by computation of the first order snake field map transport matrix [essentially that of a drift, Eq. (6)]; nonlinear field components—thus their feed-down—are weak (Eq. (3); (iii) the local vertical orbit bumps, designed to center the helix along snake axes (Fig. 11), do introduce coupling (Table II, column 2), a feed-down from chromaticity sextupoles in the bump regions (a contribution of about a third to the 0.007 coupling strength value) and from the sextupole component of main bend coil ends at injection energy (a two-third contribution). This coupling needs to be corrected as its strength is commensurate with, if not greater than, the fractional tune values; (iv) with field maps at their optimal individual setting (such that individual snakes yield $\mu = 180°$, $\phi = \pm 45°$), and adding a local vertical closed orbit bump for helix centering, the spin closed orbit $\vec{n}_0(s)$ is no longer vertical, it features a tilt from vertical around the ring (Fig. 15).

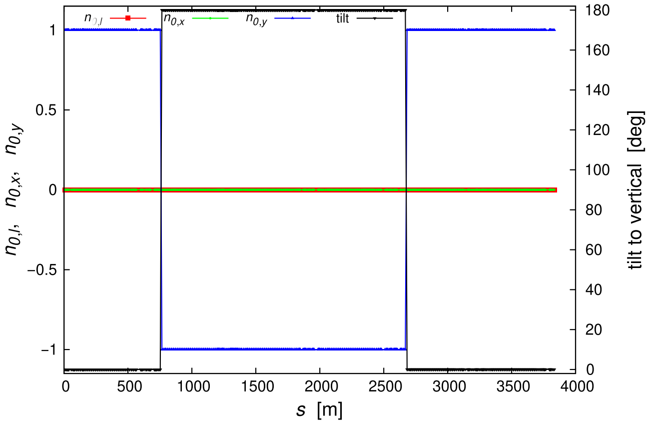

FIG. 14. Spin $\vec{n}_0$ vector around Yellow ring and tilt angle. Case of snake field maps offset, thus no orbit bumps, with helix currents $I_{\mathrm{out}} = 93.35$ A, $I_{\mathrm{in}} = 321.87$ A. Spin closed orbit is vertical around the ring.

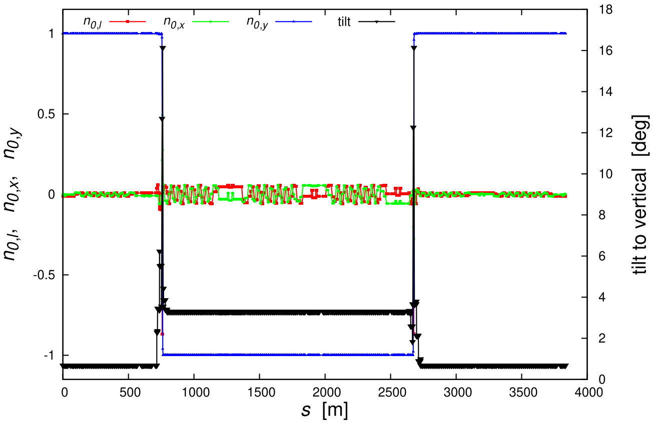

FIG. 15. Spin $\vec{n}_0$ vector around Yellow ring and tilt angle. Regular polarized proton injection optics, snake field maps, and orbit bumps in place, helix currents as in Fig. 15. The spin tilt to vertical reaches 3.5° in the arcs.

B. Store optics—255 GeV

Store optics here includes vertical orbit separation bumps at IPs, as well as local helix centering orbit bumps at

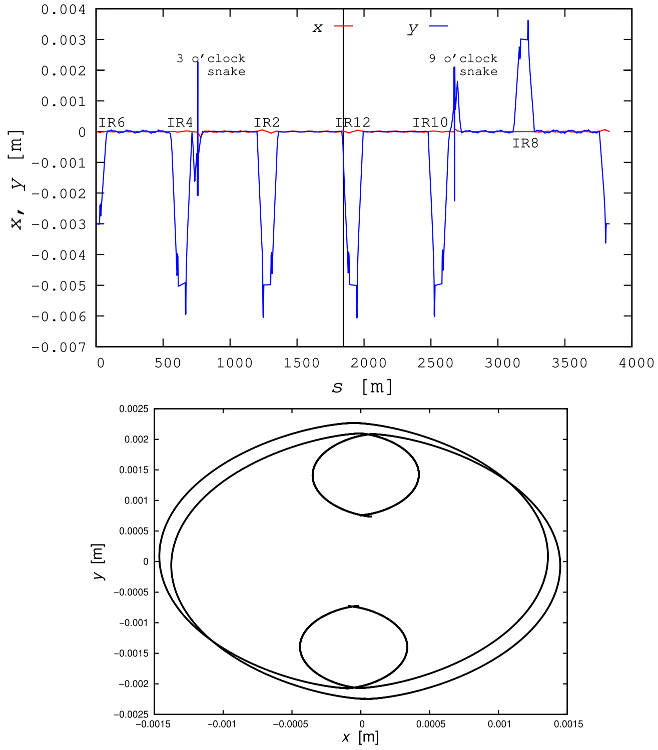

FIG. 16. Top: typical closed orbit with vertical separation bumps at IPs, in RHIC Yellow lattice nominal lattice, accounting for snake fields, at store (255 GeV); the vertical bar locates the p-C polarimeter, at $s = 1846$ m from IP6, CCW. Bottom: transverse projection of helical orbits in snakes.

snakes. Resulting orbits around the ring, and through the snakes, are given in Fig. 16. Snake-induced orbit perturbation is small enough at high rigidity (helix amplitude in snakes is down to about ±2 mm, Figs. 7, 16), that it can be taken care of by the orbit feedback during RHIC operation. Introducing snake fields in the lattice does not cause noticeable perturbation of betatron functions which essentially remain as in Fig. 10.

It can be seen from Fig. 17 that the spin tilt reaches 18° in the fall or rise regions of the orbit separation bumps. The RHIC Carbon-target "p-C" polarimeter is located in the lattice at $s = 1846$ m relative to IP6 (see Fig. 16) according to current RHIC Yellow models; the $\vec{n}_0$ tilt at that location is about 3°, whereas 7–8° have been measured.

An error in the separation bump may be the cause. The p-C polarimeter is in the rising region of the separation bump, thus any error in the beam positioning could create a larger than expected tilt angle. The transverse beam position in RHIC is controlled largely by specifying target BPM readings to an orbit feedback system. Any error in the BPM reading (e.g., from survey misalignment or deviation of the pickup's electrical center) could therefore result in orbit corrector settings (and therefore spin rotations) that differ from idealized calculations.

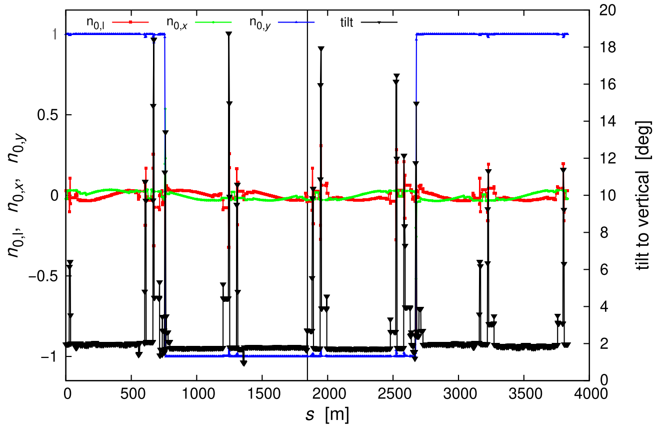

FIG. 17. Nominal RHIC Yellow ring settings, at store. The graph displays spin $\vec{n}_0$ components and tilt to vertical. The latter is about 2° around the ring, with up to 18° spikes at the fall or rise of the vertical orbit separation bumps. The vertical bar at $s = 1850$ m materializes the location of the p-C polarimeter, 1846 m from IP6, CCW, $\vec{n}_0$ tilt to vertical there is ≈3°. Snake field maps are used here.

IV. BLUE RING SNAKES RECONFIGURATION AFTER 2021 ACCIDENT

During the startup of RHIC Run 22 (December 2021), two successive power dips caused the RHIC Blue ring 9 o'clock snake to lose two of its four helices. It has been possible to maintain near-180° snake precession though (it is not possible to reach 180° with two helices, see below), by proper powering of the remaining two helices in an "R-0R + 0" series (first and third helices powered in series, second and fourth out of service). Subsequently, by a slight retuning of the 3 o'clock sister snake, near-vertical spin closed orbit $\vec{n}_0(s)$ around the ring was obtained, as well as spin tune close to ½, so preserving beam polarization during the acceleration ramp from injection to store energy. An accurate determination of the new snake settings required the use of field maps. The methods and outcomes of this work are discussed in the following.

A combination of two 360°-twist helices cannot yield a full-strength Siberian Snake. This transposes in the fact that the necessary condition for a $\mu = \pi$ spin rotation,

$$\chi^2 + \cos\left(2\pi\sqrt{1+\chi^2}\right) = 0 \tag{8}$$

has no solution [13, p. R181].

Considering RHIC identical helices with opposite fields, theoretical spin rotation μ by the helix doublet satisfies

$$\cos\frac{\mu}{2} = \frac{\chi^2 + \cos\ 2\pi\sqrt{1+\chi^2}}{1+\chi^2} \tag{9}$$

and the precession axis is in the median plane, parallel to

$$\left(\frac{2\chi}{1+\chi^2}\sin\pi\sqrt{1+\chi^2},\ \frac{2}{\sqrt{1+\chi^2}}\cos\pi\sqrt{1+\chi^2},\ 0\right). \tag{10}$$

The theoretical closest approach to $\cos\frac{\mu}{2}=0$ (*i.e.*, $\mu=\pi$), at $G\gamma=45.5$, is with $\chi=1.0225$, yielding $B_0=4.569$ T (that would be a 360 A helix current), and $\mu=172.14$ deg, with rotation axis parallel to (after Eq. (8)

$$(\text{rad, long, vert}):\ (0.9759, 0.3034, 0) \tag{11}$$

in the median plane at -55.6 deg to the longitudinal axis. Numerical optimization of a R-0R + 0 double-helix series, using field maps, yields very similar quantities, this is summarized in Table IV. On the other hand, there is a practical limit to helix current: it should not exceed 322 A, subsequent practical parameter values are given in Table IV as well. Numerical integration through this two-helix partial (90%) snake, at any energy in 23–250 GeV, yields a spin matrix of the form

$$R_{\text{sp}}\approx\begin{pmatrix}-0.11 & -0.97 & 0.22\\ -0.97 & 0.15 & 0.20\\ -0.22 & -0.20 & -0.95\end{pmatrix} \tag{12}$$

which is slightly perturbed compared to that of a four-helix full snake, Eq. (7). This spin matrix yields a snake rotation axis of

$$(\text{rad, long, vert}):\ (0.755, -0.656, 0) \tag{13}$$

at 58° from the optimal direction [Eq. (11)]. The transport matrix on the other hand remains close to that of a drift [Eq. (6)], over the 23–250 GeV energy range.

TABLE IV. Required field setting in 9 o'clock two-helix snake (columns 2, 3) and in 3 o'clock outer helices (columns 4, 5), resulting helix excursion, snake angles μ, ϕ, snake strength, spin closed orbit $\vec{n}_0(s)$, and spin tune ν_{sp}, in three different approaches at injection energy ($G\gamma=45.5$), namely, "theor.": a closest approach to Eq. (8), yielding μ [Eq. (9)] and ϕ [Eq. (10)] and, for comparison, "optim.": optimized field value using field maps; "prac.": actual RHIC operation parameter values. Columns 3 and 5 list parameter values when energy is set to 255 GeV ($G\gamma=487$) which changes helix excursion in snakes. The $\vec{n}_0$ vector around RHIC, its tilt to vertical at injection point ("inj. pt"), STAR detector and p-C polarimeter, as well as spin tune ν_{sp}, are for the four-helix case.

		9 o'clock snake parameters (two-helix)		3 o'clock snake parameters (four-helix)	
$G\gamma$		45.5	487	45.5	487
B_0	theor	4.569			
	optim [T]	4.561		1.74	
	prac	4.08		1.74	
Helix excursion [mm]		23	2.2	23	2.2
Spin prec. μ [deg]		172.1			
		171.7			
		162.3	162.5	163.8	164.0
Axis angle ϕ [deg]		−55.6			
		−66.4			
		−49.0	−48.9	+40.0	+39.9
Snake strength		90%		91%	

		Polarization (four-helix case)	
		Injection energy	Store energy
$\vec{n}_0(s)$ vector		see Fig. 18	
$\vec{n}_0$ tilt [deg]	at STAR	7	14.3
	at inj pt	7	14.3
	at p-C pol	17	7
Spin tune ν_{sp}		0.4971	0.4902

At 322 A in the 9 o'clock R − 0R + 0 partial snake, the spin rotation axis [Eq. (13)] is at −49° to longitudinal, this requires adjusting the 3 o'clock full-snake in order to maintain a 90° angle between the two snake axes (thus, spin tune closest to ½), a ≈4° adjustment. The latter condition is achieved with $I_{\text{out}}=130$ A, (a 30% current increase) and $I_{\text{in}}=322$ A (unchanged). This makes 3 o'clock a partial snake though (91%), its new parameters are summarized in Table IV, columns 4 and 5, the resulting spin closed orbit and its tilt to vertical are displayed in Fig. 18.

Comparing to nominal RHIC ring configuration (as in Sec. III, with typical $\vec{n}_0$ orientation at injection and store energies displayed in Figs. 15 and 17, respectively), Fig. 18 shows a strong perturbation under the effect of this partial snake. At injection energy, spin $\vec{n}_0$ tilt is about 7° in RHIC Blue ring injection septum region, spin tune is $\nu_{\text{sp}}=0.4971$. At store energy, the spin tune is $\nu_{\text{sp}}=0.4902$ and the spin $\vec{n}_0$ tilt is 14.3° at the STAR detector, it reaches a similar amount in the arcs, and spikes up to 27° at the fall or rise of the vertical orbit separation bumps.

Beam energy has a direct effect on spin precession via $G\gamma$, and in turn on $\vec{n}_0$ orientation around the ring, as shown in Fig. 19. During RHIC Run 22, the large spin tilt at store energy caused by the partial snake operation could be substantially reduced at STAR and at the p-C polarimeter (less than 1° tilt was measured in the latter) by lowering the energy to 254.2 GeV (from a nominal near-255 GeV with full snakes), only leaving a residual longitudinal component at both the p-Carbon location and STAR IP. Figure 19 was the base for an energy scan done to explore the spin tilt as a function of beam energy. Numerical simulations and experimental results both show that the optimal energy for the least longitudinal component is near 254.2 GeV, so providing a strong validation for the simulation methodology.

Closed orbit—An ancillary issue experienced in RHIC, at injection, with a two-helix snake, is the greater vertical

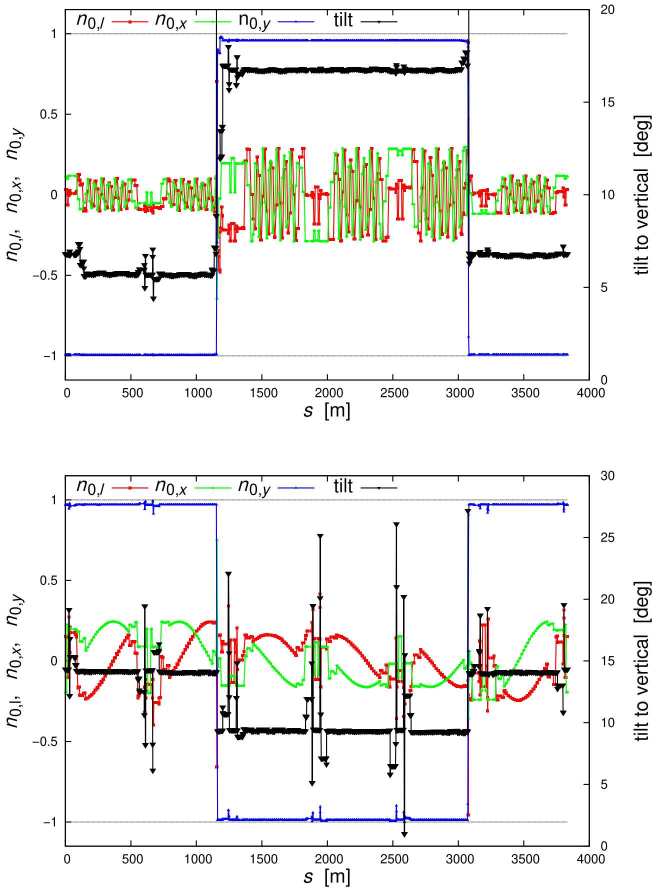

FIG. 18. RHIC Blue ring with 9 o'clock (two-helix, 90%) and the 3 o'clock (four-helix, 91%) partial snakes. The graphs show the spin $\vec{n}_0$ components and tilt to vertical around the ring at injection (top) and store (bottom) energies. The 9 o'clock snake OPERA map current is $I_{2\text{-hlx}} = 322$ A, the 3 o'clock snake currents are $I_{\text{out}} = 130$ A, $I_{\text{in}} = 322$ A.

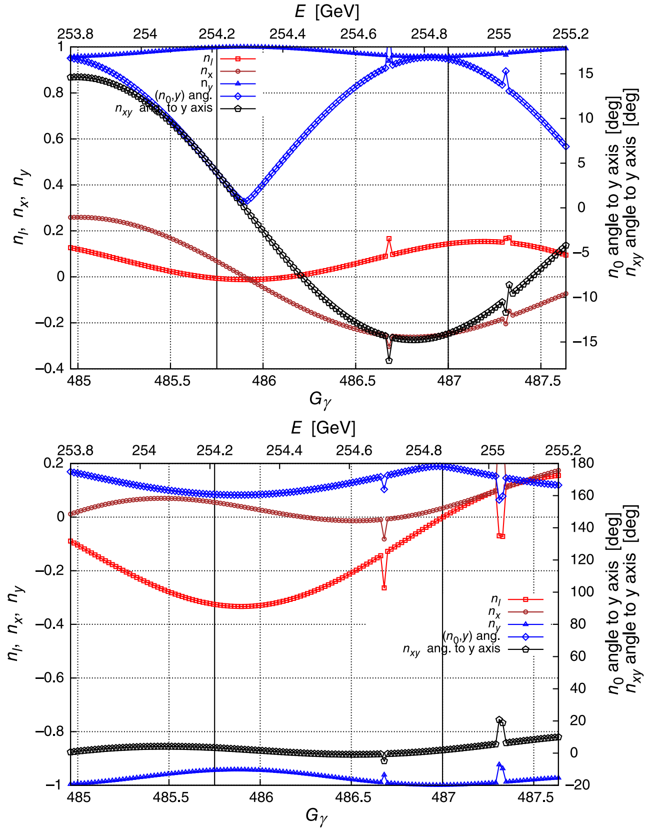

FIG. 19. Energy dependence of $\vec{n}_0$ components (left axis) and $\vec{n}_0$ angle to the y axis (right axis) at STAR (top) and at p-C polarimeter (bottom); n_{xy} denotes the modulus of the projection of $\vec{n}_0$ in the (x, y) plane, which is the vector actually measured at the p-C polarimeter [14]. The right vertical bar at $G\gamma = 487$ materializes the region of nominal operation with full snakes. The left vertical bar at $E = 254.2$ GeV was the optimal energy found from measurements, for operation with partial snake during RHIC Run 22, which this graph shows to be close to the expected energy value for a zero-tilt to vertical. Snake field maps are used for this energy scan.

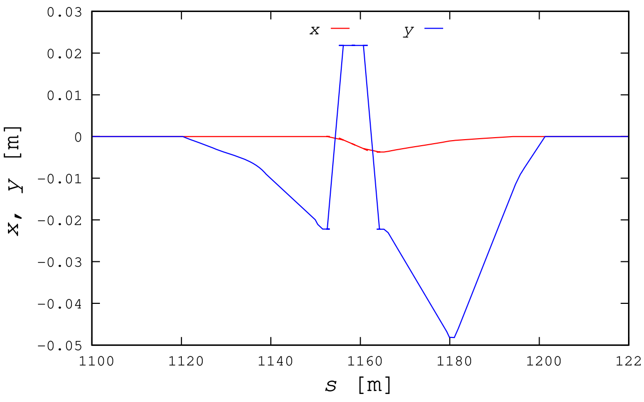

FIG. 20. Vertical local closed orbit bump in the two-helix snake region, at injection, using the helix field maps.

excursion of the local closed orbit bump (downstream of the snake, due to a focusing quadrupole, Fig. 20) compared to regular operation (Fig. 12). The reason is that the snake helix entrance and exit position is greater with two helices, ≈23 mm (Fig. 21) versus ≈9 mm with a four-helix snake (Fig. 7). During RHIC Run 22 the effect was mitigated with a nonzero closed orbit incidence at the entrance and exit of the snake, resulting in a better balanced ≈± 30 mm excursion in the snake region, down from an otherwise −49 mm extreme.

Crossing strong resonances—Four strong intrinsic resonances are crossed during the acceleration ramp from injection $G\gamma = 45.5$ to store energy in the 250 GeV region. As detailed in Sec. II, snake parameters only weakly depend on beam rigidity and helical excursion across the snake, as a consequence injection settings are used for the assessment of polarization preservation during resonance crossings. The acceleration process was simulated by tracking 1000 particles with transverse Gaussian distributions, with normalized emittances $\epsilon_x = \epsilon_y = 2.5\ \pi\mu$m, and

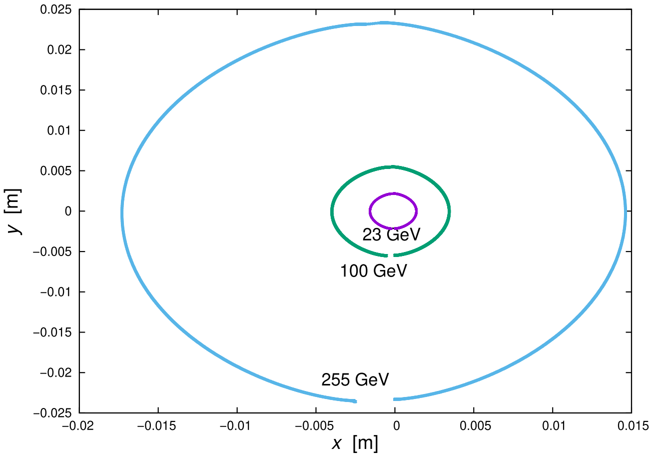

FIG. 21. Transverse projection of the helical motion across a two-helix snake field map, at various energies.

relative momentum spread $\sigma_{\delta p/p} = 5\times10^{-4}$, corresponding to the nominal RHIC values. All initial spins are vertical, consistently with the simulated $\vec{n}_0$ transfer function from AGS to RHIC Yellow injection kicker (Fig. 22) [15].

Figure 23 displays the evolution of polarization through the strongest resonance, $G\gamma = 393 + \nu_y$, crossed in about 20,000 turns at an acceleration rate of 200 kV/tun (about 10 times the actual rate). The graphs show different polarization at the start (i.e., a different average $\langle S_y\rangle$ over the 1000 particles tracked), which is an effect of the difference in $\vec{n}_0(s)$ spin closed orbit between the partial snake and full snake cases. The upper polarization value in the partial snake case, ≈95%, is consistent in particular with the ≈14.3° tilt of $\vec{n}_0$ at STAR (the origin in this tracking) at store energy (Table IV and Fig. 18).

Operation-wise, the partial snake configuration with the 9 o'clock snake current set to 320 A and the 3 o'clock snake inner and outer currents set to 130 and 322 A, respectively, showed no indication of increased polarization loss during the RHIC acceleration ramp; beam polarization reached 53% at store in Blue, the same performance as in Yellow and similar to the previous, 2017, RHIC polarized proton runs [16,17]. These simulations played an important role in designing the new local orbit bump following the incident, and to support this partial snake setting as an effective alternative for beam polarization preservation during RHIC Run 22.

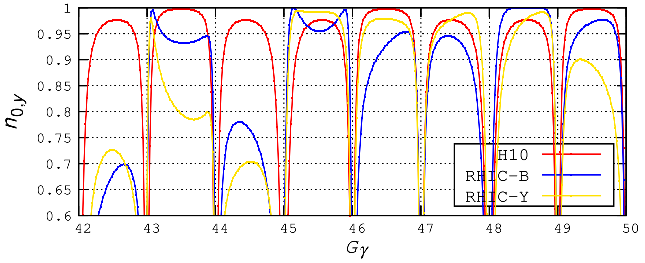

FIG. 22. Transmission of $\vec{n}_0$ from AGS H10 extraction septum to RHIC injection kickers, over the range $G\gamma \in [42, 50]$, from numerical simulation. The graph displays $\vec{n}_{0,y}(G\gamma)$ at three different locations: H10 and the RHIC Blue and Yellow ring kickers. In this simulation, the periodic spin precession axis $\vec{n}_0(G\gamma)$ at the extraction septum in the AGS ring is computed using the AGS partial snakes OPERA field maps [15].

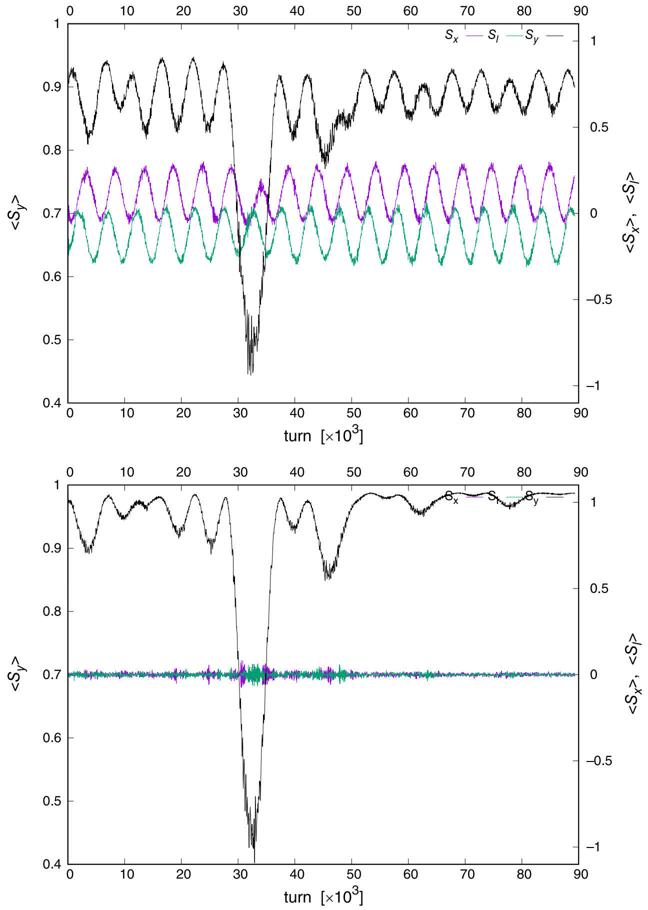

FIG. 23. Turn-by-turn $\langle S_y\rangle$ (left axis), $\langle S_x\rangle$ and $\langle S_l\rangle$ (right axis), an average over 1000 particles, during the crossing of the intrinsic resonance $G\gamma = 393 + \nu_y$, at a rate of 200 kV/turn. Observation point is IP6. All initial spins are vertical, whereas $\vec{n}_0$ is not. Top: a case of 90% 9 o'clock snake (two helices) and 91% 3 o'clock snake (four helices); nonzero $\langle\langle S_x\rangle\rangle$ and $\langle\langle S_l\rangle\rangle$ turn averages reflect $\vec{n}_0$ tilt. Bottom: both snakes are full snakes (four helices).

V. ROTATORS

Spin rotators are located on both sides of IP6 and IP8 in RHIC (Figs. 2, 24), they are used to move the spin closed orbit $\vec{n}_0$ to the appropriate direction at the IPs: for longitudinal orientation, for instance, a rotator moves $\vec{n}_0$ into the horizontal plane, while the D0 and DX separation

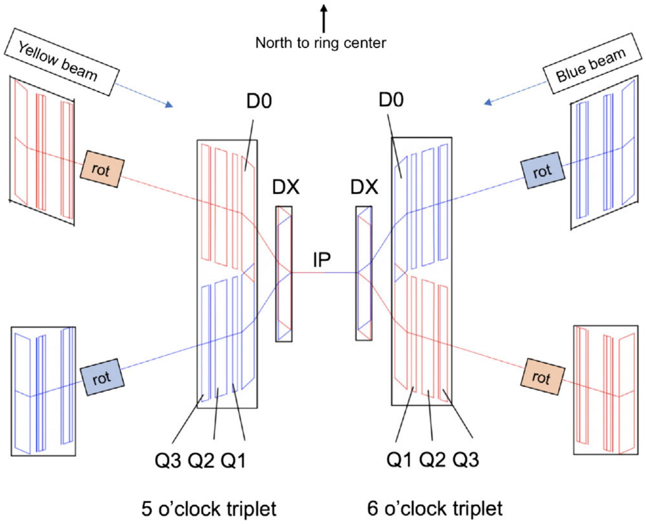

FIG. 24. Rotator pairs at IP6 in RHIC.

dipoles located between rotator and IP provide a complementary y-axis rotation to longitudinal.

RHIC rotators are a series of four 360°-twist helices, with the same layout as RHIC snakes (Fig. 3), yet with alternate right (R) and left (L) helicity, and magnetic field oriented radially at helix ends. Referring to Fig. 2, simulation-wise RHIC rotators are modeled by the following series (+/− stands for positive/negative helix current in the OPERA helix model):

$$\begin{array}{ll} \text{Yellow (CCW)}: & \text{Blue (CW)}: \\ \mathrm{L+R+L+R+} & \mathrm{R+L+R+L+} \\ \mathrm{L-R-L-R-} & \mathrm{R-L-R-L-} \end{array}$$

Field maps—The 360°-twist rotator right- and left-handed helix field maps, with end fields radial [Eq. (14)], are derived from snake ones.

Outcomes are illustrated with graphs of the field experienced across left-handed high-field (outer) and a right-handed low-field (inner) helices in Fig. 25; they are consistent with Eq. (14) for $B_0 > 0$ and helicity $\epsilon = \mp 1$, respectively, yet the radial field component departs noticeably from $\cos(ks)$ at magnet ends, this may be expected to yield optimal helix field settings departing slightly from theoretical values drawn from Eq. (1). Additional details can be found in Table V.

In RHIC rotators, comprised of four helices with alternate handedness and designed for orbit transparency, the overall rotation axis lies in the transverse plane (x, y) (whereas the individual helix rotation axis is in the (x, s) plane, details in Table V), at an energy dependent angle $\theta = 10$–$45°$ to the radial axis; spins precess from vertical into the horizontal plane (or vice-versa) by an energy dependent angle $\mu \approx 90$–$100°$. Note that in addition the D0 and DX orbit separation magnets, located between rotators and IP (Fig. 24), contribute a final ≈10–100° energy dependent y-rotation that completes the alignment of the $\vec{n}_0$ vector along the longitudinal axis at the IP. To achieve proper θ and μ values, the field in outer helices is 2.1 T at 25 GeV, up to 3.5 T at 250 GeV; in inner helices, the field is within 2.8–3.1 T in that energy range. Given these field values, high field OPERA maps (computed with $I_{\mathrm{out}} =$ 322 A current, 4 T field, see Sec. II) are used to simulate all four rotator helices.

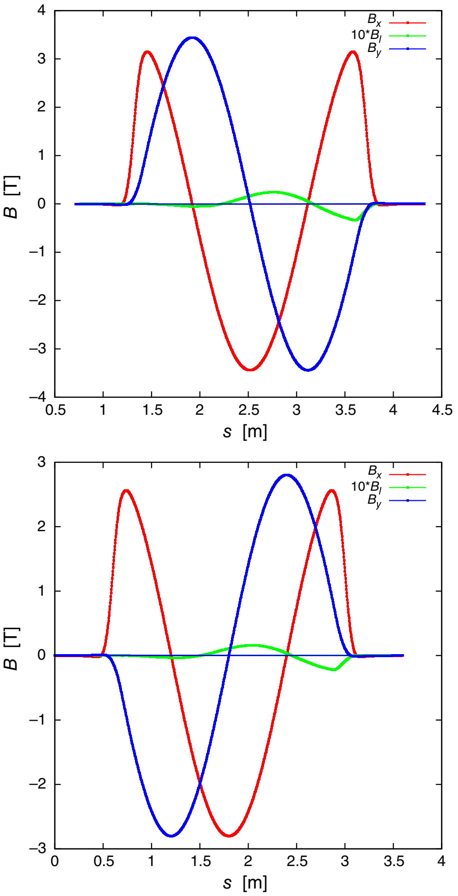

FIG. 25. Field along RHIC closed orbit across a 360°-twist rotator helix. Top: outer "L+" left-handed helix ($k < 0$, $B_0 > 0$). Bottom: inner "R+" right-handed helix ($k > 0$, $B_0 > 0$).

Theoretical expectations—The theoretical field in a rotator helix is, to order zero in the transverse coordinates x, y (see Eq. (3)

$$\begin{cases} B_x = B_0 \cos(ks) \\ B_y = -B_0 \sin(ks) \end{cases} \tag{14}$$

with the helicity determined by the sign of k (Eq. (4). The spin rotation axis through a 360°-twist helix is (with χ as

TABLE V. Spin parameters of RHIC Yellow rotator 360°-twist helix, of the LRLR series, and of RHIC ring, including precession axes, "prec. axis" (radial, longitudinal, vertical). Data listed are either from theory or from simulations using field maps, as specified.

$B\rho$ ($E = 255.2$ GeV)	(T m)	851.25	
Field map data:			
		Outer helices	Inner helices
Current	(A)	263	211
Field B_0	(T)	3.45	2.80
		Helix, from theory and from field maps:	
		L± and R±	L± and R±
χ (Eq. (1)		0.7564	0.6139
Prec. axis (Eq. (15))		(−0.603, 0.798, 0)	(0.523, −0.852, 0)
Prec. axis (maps)		(−0.595, −0.804, 0)	(−0.51, 0.858, 0)
Spin rotation μ (Eq. (1)	(deg)	91.4	62.43
Spin rotation (maps)	(deg)	89.42	61.39
		LRLR rotator series, using field maps:	
		L + R + L + R+	L − R − L − R−
$\vec{n}_0$ motion		vert. to long.	long. to vert.
Prec. axis		(−0.7143, 0, −0.700)	(0.7163, 0, 0.698)
$\vec{n}_0$ rotation to mid-plane	(deg)	158.7	163.1
$\vec{n}_0$ y-rotation in D0-DX	(deg)	102.2	102.6
		RHIC Yellow ring, using the 16 snake and rotator maps:	
$\vec{n}_0$ vector at IP6		(−0.008, 0.99996, −0.004)	
$\vec{n}_0$ angle $\vec{s}$ axis at IP6	(deg)	0.52	
Spin tune		0.48473	

defined in Eq. (1), and $\epsilon = \pm 1$ for respectively right or left helicity)

$$(\text{rad}, \text{long}, \text{vert}) \colon \left(\frac{\epsilon\chi}{\sqrt{1+\chi^2}}, \frac{-\epsilon}{\sqrt{1+\chi^2}}, 0\right) \qquad (15)$$

lying in the horizontal plane, (x, s). The graphs in Fig. 26 show the rotation of an initially vertical spin across L+ and R + helices, in the case of optimized field settings for longitudinal alignment of the $\vec{n}_0$ vector at IP6 in RHIC (see Sec. VI). Additional details regarding L± and R± rotator helix parameters are given in Table V.

Optically, a rotator transfer matrix at store energy is essentially that of a drift, like snakes. Ring optical functions are thus expected to be left unperturbed (Fig. 10) when inserting rotators.

TABLE VI. RHIC Yellow lattice, including field maps of snakes and STAR rotators. Optical parameters at store energy.

	23.8 GeV	255 GeV
ν_x, ν_y	28.697, 29.690	28.691, 29.685
$x_{\text{co}}, y_{\text{co}}$ max. (mm)	0, 0	3.8, 6
η_x, η_y max. (m)	1.88, 0	1.95, 0.15
β_x, β_y max. (m)	144, 143	1585, 1070

VI. RHIC YELLOW WITH SNAKES AND ROTATORS

RHIC Yellow ring lattice in this section includes the sixteen field maps of the 9 o'clock and 3 o'clock snakes, and STAR rotators, the latter set for longitudinal spin $\vec{n}_0$ at IP6 at 255 GeV. Basic optical parameters at injection and top energies are given in Table VI. Top energy is considered in the following, with vertical separation bump at IP6 zero-ed.

Uncorrected horizontal and vertical closed orbits excited by the rotators are displayed in Fig. 27, together with the compensation of the defect by local orbit bumps at rotators, as for the snakes. Note that during operation the orbit feedback system takes care of compensating the snake and rotator small (mm range) orbit defect. Inserting the rotators leaves the ring optics essentially unchanged (as in Fig. 10).

Figure 28 shows the local closed orbit bumps at the two rotators. Both bumps are designed using two horizontal and two vertical existing kickers in the lattice (incidentally, this may not strictly reproduce the actual orbit during RHIC operation). A fitting procedure takes care of satisfying the four orbit constraints: horizontal and vertical orbits locally

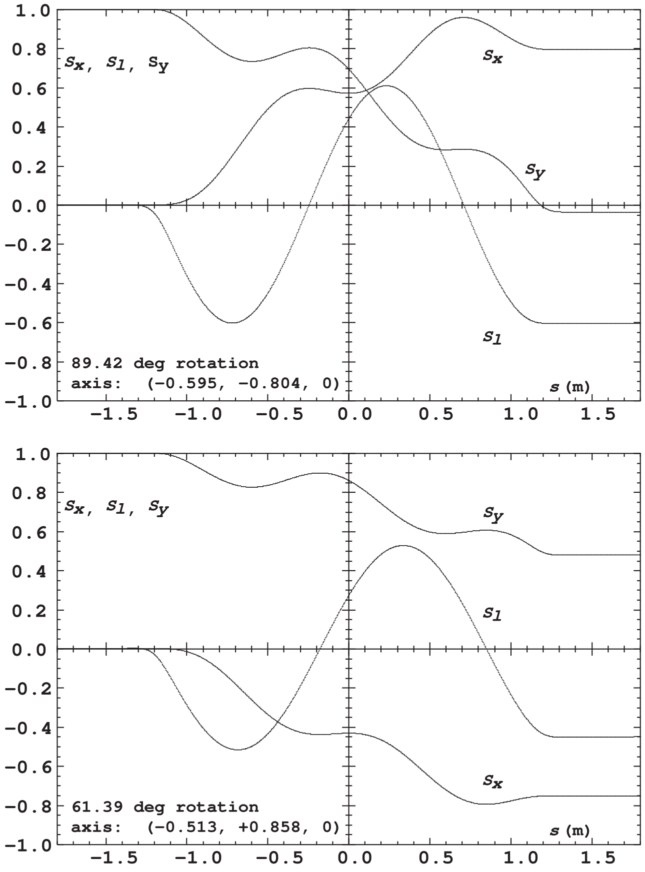

FIG. 26. Rotation of an initially vertical spin, along the closed orbit across a 360°-twist rotator helix. Top: L+ left-handed helix. Bottom: R+ right-handed helix.

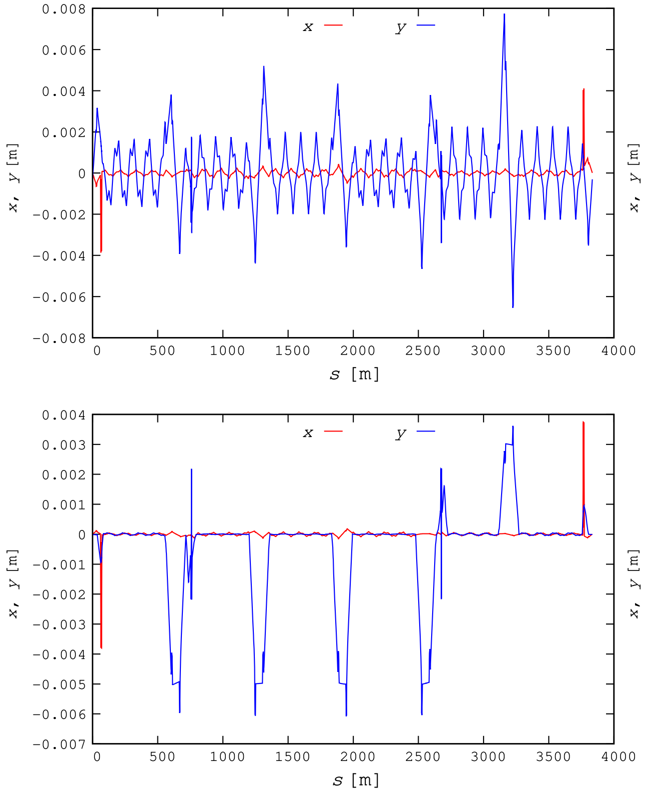

FIG. 27. RHIC Yellow ring, 255 GeV. This lattice includes the 16 OPERA field maps of the 9 o'clock and 3 o'clock snakes, and STAR rotators, the latter set for rotation of spin $\vec{n}_0$ to longitudinal at IP6. Origin of s is at IP6, location of the STAR detector. Top: closed orbit excited when introducing the 16 field maps in the lattice, prior to correction. Bottom: after correction, based on local closed orbit bumps at both rotators and both snakes.

zeroed; it also fits the spin constraints of having a vertical spin $\vec{n}_0$ at the end of the local bump, given a longitudinal $\vec{n}_0$ at IP6.

A comparison of spin rotation parameters in the rotators with theoretical expectations [Eq. (15)] is detailed in Table V. Various more or less small discrepancies need to be surmounted to achieve optimal polarization settings, which if not can accumulate and yield (i) perturbed spin tune which can be detrimental to the polarization lifetime. For example, vertical local orbit bumps at the snakes were observed to shift the spin tune to $\nu_{sp} = 0.48657$ during operations. This was corrected by adjusting the snake settings away from the theoretical values slightly. The use of pure spin rotations in absence of the orbital effects will not capture this effect (spin flipper experiments during RHIC 2017 run (Run 17) have allowed measuring the spin tune, $\nu_{sp} = 0.496$, quite close to the required $\nu_{sp} = ½$ value [18,19]); (ii) misalignment of $\vec{n}_0$ at the IP. For example up to 15° misalignment has been observed in RHIC and we are currently investigating the causes; (iii) different beam polarization in RHIC Blue and Yellow rings as observed for many years (up to 10%, relative), and despite the fact that according to BPM measurements, orbit rms errors are comparable. The ultimate source of this discrepancy is still to be determined.

Polarization—To conclude this study, Fig. 29 shows the polarization achieved with the optimal settings and resulting orbit and spin data listed in Table V. In spite of the above efforts for snake and rotators optimization, it can be observed that imperfections remain, such as the aforementioned $\nu_{sp} \neq ½$, up to 20° vertical tilt of the spin closed orbit at IP separation bumps, 4° in the arcs, etc. And things can be expected to not be as good in real life, where adjustments and measurements are far more delicate than in computer simulations.

In relation to the aforementioned issue of spin tilt at STAR observed during RHIC polarized proton runs, Fig. 29 also displays details of $\vec{n}_0$ components in the IR6 region, from vertical spin at YI6_B3 rotator entrance (at $s = 0$ in this graph) to longitudinal at IP6 ($s \approx 77$ m). With the present settings, outcomes are quasiperfect,

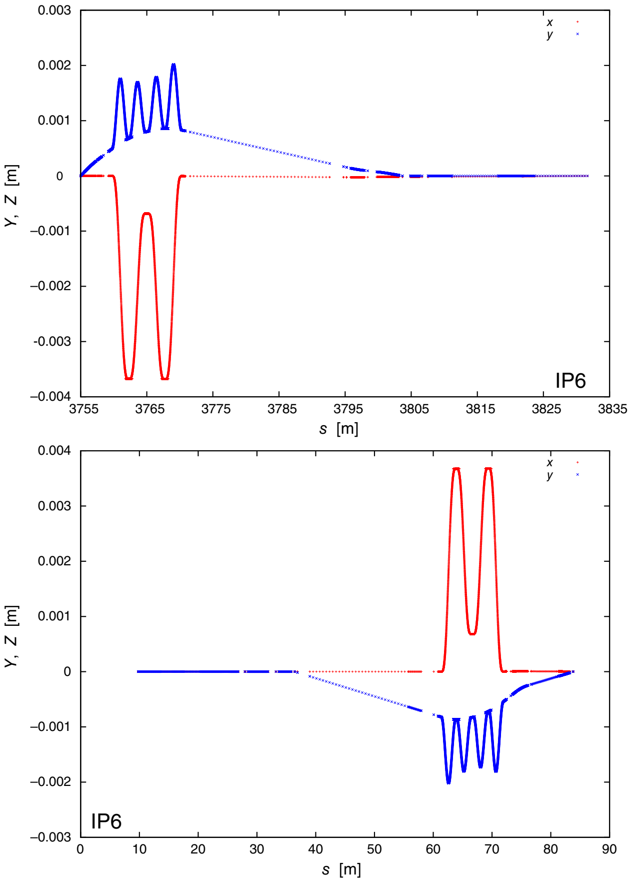

FIG. 28. Local horizontal (red) and vertical (blue) closed orbit bumps in the IP6 (STAR) rotators in the present simulations, using OPERA field maps. IP6 (STAR) is at $s = 0$, increasing s is CCW. Top: $L + R + L + R+$ rotator, upstream of IP6, moves spin $\vec{n}_0$ from vertical in the arc to longitudinal at IP6. Bottom: $L - R - L - R-$ rotator downstream of IP6, moves spin $\vec{n}_0$ from longitudinal at IP6 to vertical in the arc.

whereas during real operations, they are not, and accurate field models are required along with tracking tools to investigate the various possible causes.

VII. SPIN TRANSPARENCY MODE EXPERIMENT

A “spin transparency” mode of operation of RHIC would allow preservation and control of ion spin polarization at store [20–22]. It makes the ring lattice “invisible” to the spin and allows for polarization control by small quasistatic magnetic fields with practically no effect on beam orbital parameters.

The method is the subject of experiments, using RHIC Yellow ring, aimed at providing data at injection to validate the principles and investigate its interest in the future Electron Ion Collider (EIC) at BNL [2]. RHIC ring (Figs. 1, 2) can be configured in the transparent spin mode by aligning the precession axes of the two Siberian snakes (located, respectively, in the 3 o’clock and 9 o’clock sextants). For this experiment, theoretical snake parameters were cross-checked in detail using field map simulations. This work permitted detailed predictions of the polarization response in this experiment.

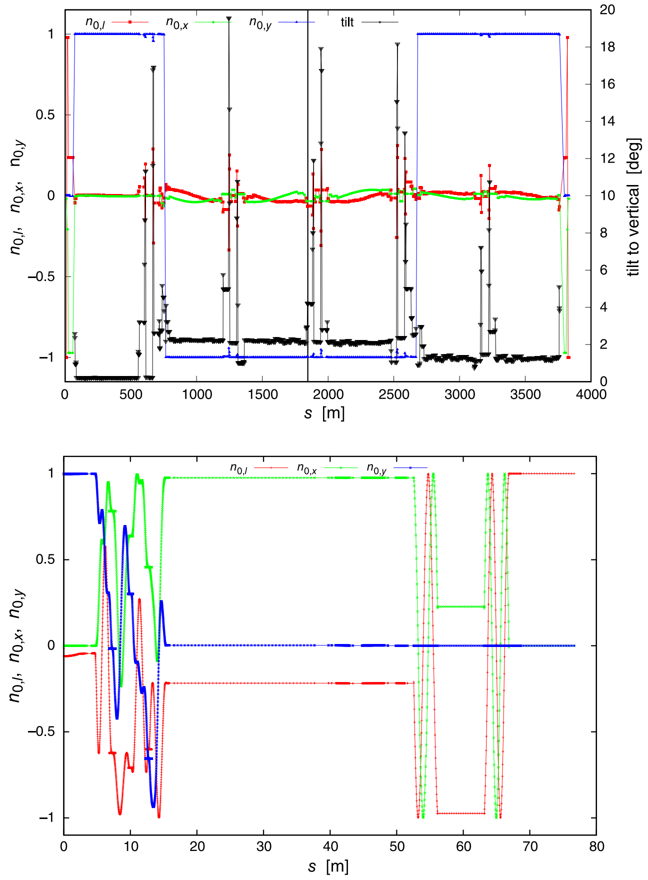

FIG. 29. Top: Polarization ($\vec{n}_0$ vector components, left axis) around RHIC Yellow ring, and $\vec{n}_0$ tilt angle to vertical (right axis). Run 22 store optics (255 GeV), the lattice includes the 16 snake and rotator field maps. The $\vec{n}_0$ tilt spikes are located at the vertical orbit separation bumps at IPs. Bottom: details of $\vec{n}_0$ components in IR6 region, from vertical spin at YI6_B3 rotator entrance (at $s = 0$ in this graph) to longitudinal at IP6 ($s \approx 77$ m).

In a first experiment, the ring polarization (technically, the $\vec{n}_0$ vector) was moved from vertical to radial, in the second one the polarization was reversed, up ↔ down. The $\vec{n}_0 = (n_{0,x}, n_{0,l}, n_{0,y})$ vector was moved by slowly changing the two snake angles, by, respectively, $\delta\mu$ and $\delta\phi$, achieving [21]

$$n_{0,x} = \frac{\delta\mu_{\text{snake}\,1} - \delta\mu_{\text{snake}\,2}}{2\pi\nu_{\text{sp}}} \sin\frac{G\gamma\pi}{2} \tag{16}$$

$$n_{0,l} = -\frac{\delta\mu_{\text{snake}\,1} + \delta\mu_{\text{snake}\,2}}{2\pi\nu_{\text{sp}}} \cos\frac{G\gamma\pi}{2} \tag{17}$$

$$n_{0,y} = \frac{\delta\phi_{\text{snake}\,1} + \delta\phi_{\text{snake}\,2}}{\pi\nu_{\text{sp}}} \tag{18}$$

The first experiment, moving $\vec{n}_0$ from vertical to radial, is addressed here. Methods for simulation of the second experiment and expected outcomes are similar [23].

A. Snake settings

The snake four-helix series in Yellow is (Sec. II)

$$\begin{array}{cc} 3\,\text{o'clock}: & 9\,\text{o'clock} \\ \mathrm{R+R-R+R-} & \mathrm{R-R+R-R+} \end{array}$$

For spin transparency, snake axes are aligned, and helix currents are in a 150–230 A range, resulting in reduced helix excursion (1.5 cm range) compared to normal operation (2.3 cm resulting from $I_{\text{in}} = 320$ A, Fig. 7). This is illustrated in Figs. 30 and 31. The respective spin transport matrices and resulting snake angles μ and ϕ for the two cases displayed are as follows:

9 o'clock snake:

```
 0.937525    -0.347918    0
-0.347918    -0.937525    0
 0            0          -1.

Spin precession: 179.9750 deg
Precession axis: (-0.1767, 0.9843, 0)
```

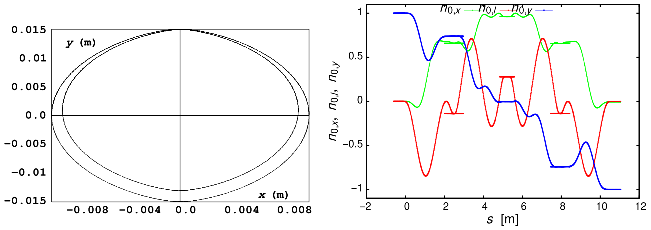

FIG. 30. Along RHIC Yellow 9 o'clock snake, case of $I_{\text{out}} = 185$ A, $I_{\text{in}} = 199$ A: $\phi = -10°$ and $\mu = 180°$. Left: transverse projection of the helical motion. Right: spin components, case of initially vertical spin (the small back-forth segments are field map artifacts).

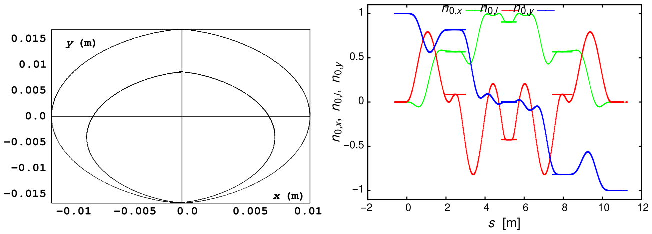

FIG. 31. Along RHIC Yellow 3 o'clock snake, case of $I_{\text{out}} = 164$ A, $I_{\text{in}} = 221$ A: $\phi = 0°$ and $\mu = 180°$. Left: transverse projection of the helical motion. Right: spin components, case of initially vertical spin.

3 o'clock snake:

```
1.00000     0.00090     0
0.00090    -0.99998    -0.00579
0           0.00579    -0.99998

Spin precession: 179.6680 deg
Precession axis: (1.0000, 0.0005, -0.0000)
```

A rotation of the spin precession axis from vertical to radial requires a time dependent, continuous change of snake angles in the range

$$\mu\colon 180° \to 164°, \quad \phi\colon 170° \to 180°, \quad \text{for the 9 o'clock snake}$$

and

$$\mu\colon\ 180° \to 165°, \qquad \phi\colon 0, \qquad \text{for the 3 o'clock snake.}$$

Stepwise changes of 11 steps have been programmed for convenience in RHIC experiments, they are displayed in Fig. 32. The resulting required I_{out} and I_{in} snake currents are obtained by fitting, based on the computation of the aforementioned spin transport matrices (constraints are matrix properties, variables are OPERA field map currents); the fit penalty is used to control convergence of the solution. It appears in particular that snake current signs for these spin transparency experiments are the same as in regular RHIC Yellow operation simulations: snake helix polarities/connections do not need to be changed—fortunately! Figure 33 shows the motion of $\vec{n}_0$ at IP6 so obtained, and the concurrent resulting evolution of $\vec{n}_0$ at the p-C polarimeter in IR12 (Fig. 1), used for polarization measurements.

B. RHIC Run22 experiments

Spin transparency experiments have been devoted dedicated operation time during RHIC Run22. They have been performed in the RHIC Yellow ring, at injection energy ($G\gamma = 45.5$). As seen in the previous section, field map settings slightly differ from the nominal operation, however, with marginal impact on lattice optics which essentially remains that of Table III and Fig. 11.

There is no need for vertical orbit recentering in the snakes during the slow change of the snake angles, as the change in orbit excursion is marginal (Fig. 34).

When it comes to defining snake power supply ramp functions for RHIC operation, the question of maintaining constant spin tune may matter—to what extent is still a pending question. In this situation, the four fitting variables are still the snake currents, however, the constraints of the four snake angles are replaced by constraints on the components of the spin $\vec{n}_0$ vector at one or more locations around the ring.

Ramps with this spin tune constraint can be worked out starting from initial snake current functions designed for

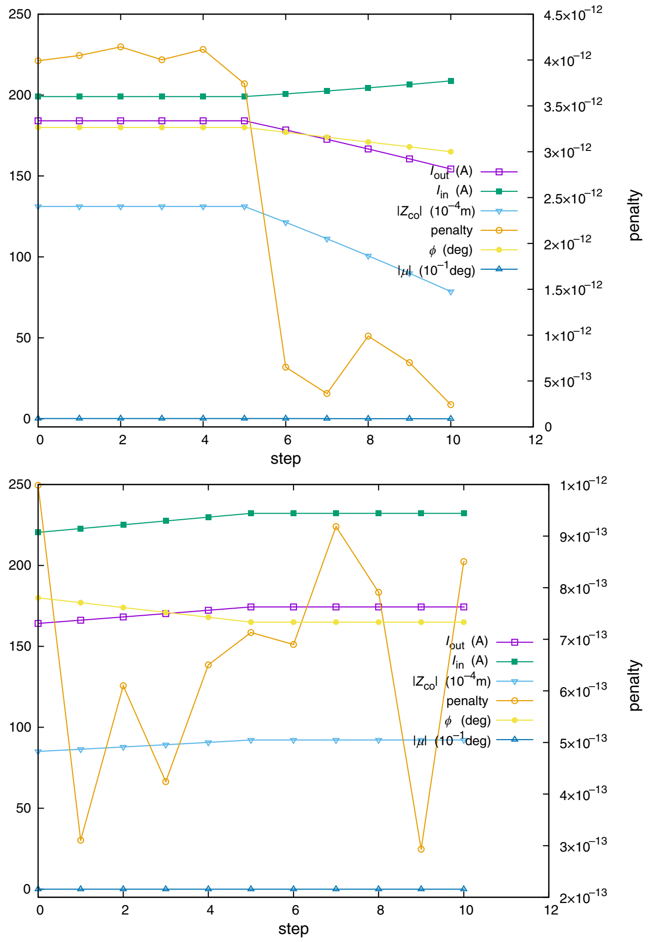

FIG. 32. Required ramp of snake angles μ and ϕ, for rotation of RHIC Yellow ring polarization from vertical to radial; OPERA currents necessary for that, obtained by constraining the snake spin matrix; resulting closed orbit coordinate at snake entrance; and monitoring the convergence of this fit: fit penalty (right vertical axis). Top: 9 o'clock snake; bottom: 3 o'clock snake. The right axis in these graphs gives the penalty function values, other quantities use the left axis.

the sole snake angle constraints as displayed in Fig. 32, varied anew ensuring the smooth evolution of the $\vec{n}_0$ and fixing the spin tune ν_{sp}.

In the tracking trial below, however, ramps as shown in Fig. 30 are used, thus the spin tune is expected to vary over

$$\nu_{\mathrm{sp}}:\ 0.0621 \rightarrow 0.0868. \tag{19}$$

In this simulation, the change in bunch polarization from vertical to radial used a linear interpolation of currents between the aforementioned 11 steps. A 1000-particle bunch is tracked over 15,000 turns including a preliminary "idle" 5000 turns to permit the stabilization of the

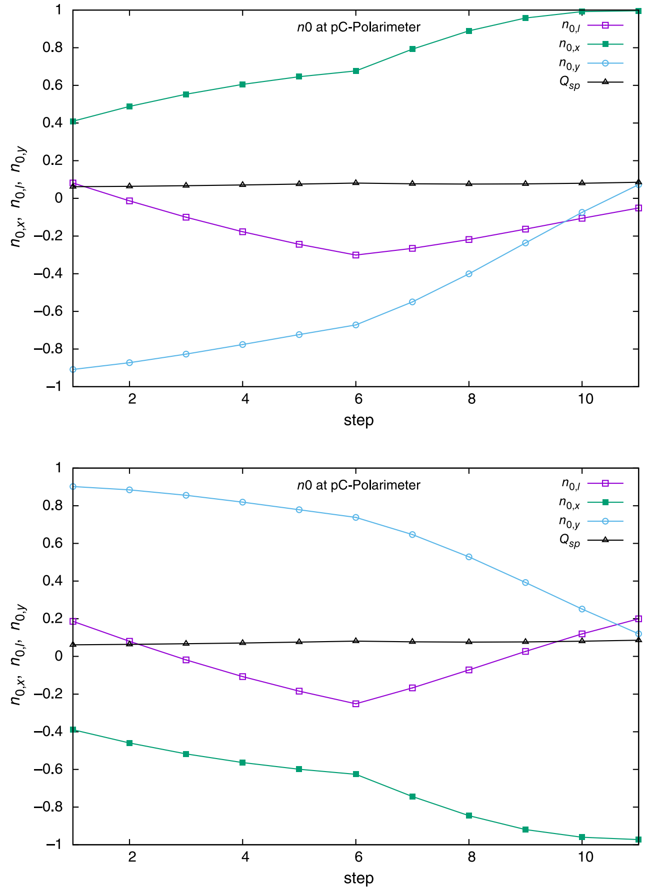

FIG. 33. Components of the stable spin precession direction, and spin tune, over the snake power supply ramp. Top: at IP6; bottom: at the p-C polarimeter, location of the polarization measurement in this experiment. Data were obtained from the one-turn spin matrix.

longitudinal beam density and polarization. Beam parameters are nominal RHIC values at injection, namely, Gaussian densities with

$$\epsilon_x = \epsilon_y = 2.5\pi\ \mu\mathrm{m}, \qquad \text{normalized;} \qquad |\delta p/p| \le 10^{-3}.$$

A double rf system was used, with frequencies and voltages 9 MHz/17 kV and 197 MHz/11 kV. The longitudinal phase space motion is displayed in Fig. 35 with the initial longitudinal 2D density matched to the stationary rf bucket. The synchrotron period at large amplitudes is about 15,000 turns which compares to the preliminary 5000 turns used to initialize the beam distribution.

The 6D simulation is displayed in Fig. 36, and bunch polarization and spin tune evolution so obtained are consistent with expectations from one-turn matrix calculation outcomes shown in Fig. 33 and in Eq. (19). Thus bunch polarization is essentially unaltered during the rotation of $\vec{n}_0$ (black curve in Fig. 36). Further simulations

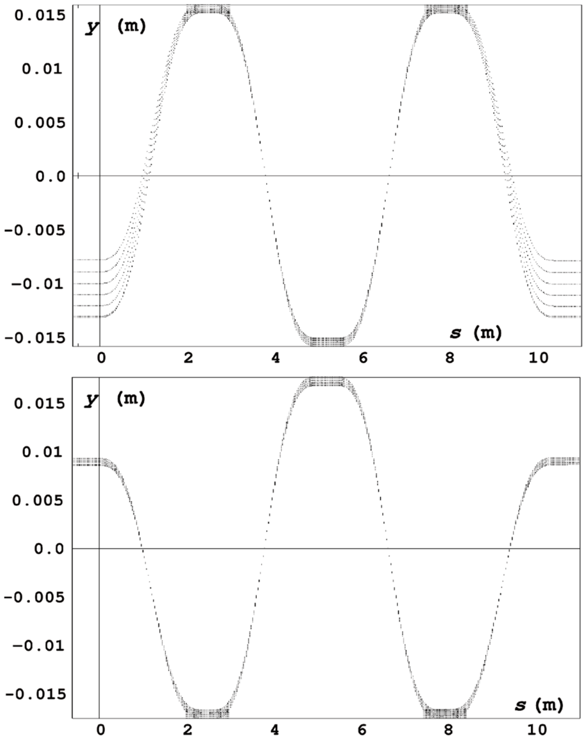

FIG. 34. Vertical closed orbits along 9 o'clock (top) and 3 o'clock (bottom) snakes, sampled over the helix current scan from vertical to radial polarization.

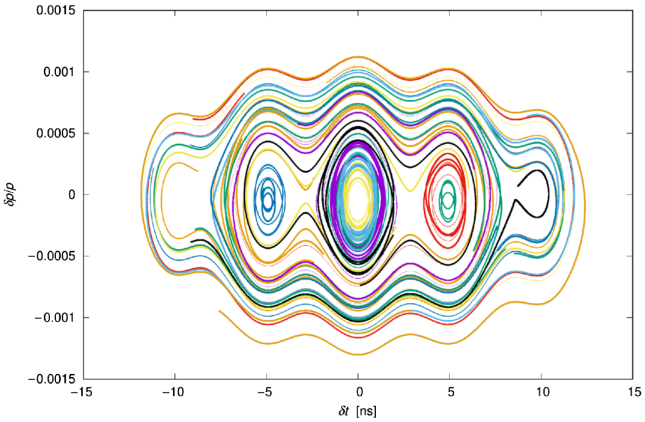

FIG. 35. Sample particle motion in longitudinal phase space over an initial 5000 turns spin and longitudinal stabilization phase, followed by 10,000 turn snake supplies ramp. Bunch length is about RHIC nominal 25 ns, momentum excursion is $\pm 10^{-3}$.

show that ramp speed is not critical, it could be faster than used in these simulations; RHIC snakes ramp is orders of magnitude slower anyway (it takes minutes).

VIII. IN SUMMARY

In a series of five sections, this paper discusses the interest in using snake field maps as optical elements proper in RHIC lattice modeling. With a glance in addition to the interest of doing so as well in RHIC injector: the AGS, as its partial snakes determine the injected spin polarization at RHIC Yellow and Blue ring injection septa.

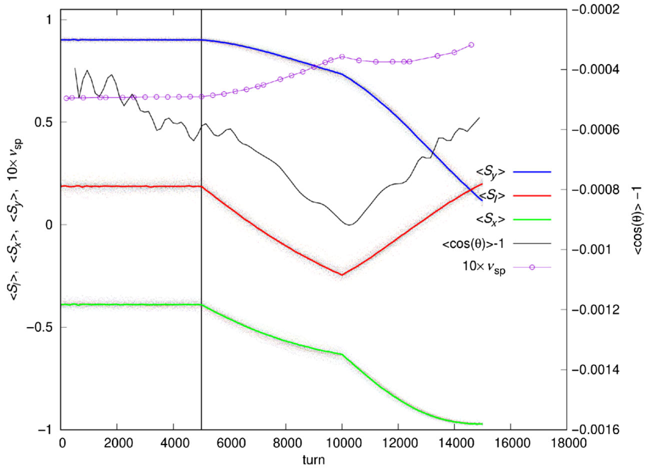

FIG. 36. Polarization rotation from vertical to radial over 10,000 turns observed at p-C polarimeter (current ramp starts at turn 5000, materialized by the vertical bar). Dots: spin components of a few individual particles; superimposed solid lines: turn-by-turn average of 1000 particle spin components. Black solid line (right axis): departure from 1 of the bunch polarization (*i.e.*, the average value of $\vec{S}_i \cdot \langle\vec{S}\rangle$, the projection of individual spins $\vec{S}_i$ on their average $\langle\vec{S}\rangle$). Empty circle markers (left axis): spin tune $\nu_{\rm sp}$, times 10, from Fourier analysis.

The interest of using field maps is in that they represent optical element modeling closest to real life: it is commonly admitted that OPERA style magnet computer codes deliver fields which are within a few percent of the fields measured in the magnets they allowed to design. The counterpart is that this requires stepwise numerical integration of particle and spin motion, as opposed to conventional first order matrix product and kick-drift modeling techniques.

The goal in the examples addressed above is mostly to show the detailed insight in spin closed orbit, and in particle trajectory which determines accuracy on the former, which the use of field maps permits. It has been shown that in several cases, they are necessary in order to understand experimental observations such as spin tune and spin closed orbit vector tilt, as well as to precisely control the effect of snakes and rotators on these two spin dynamics parameters which are paramount in controlling and preserving beam polarization. Various publications address these questions and can be referred to for additional details [2,3,12,14–16,21–23].

ACKNOWLEDGMENTS

This research used resources from the National Energy Research Scientific Computing Center (NERSC), a U.S. Department of Energy Office of Science User Facility located at Lawrence Berkeley National Laboratory. Work supported by Brookhaven Science Associates, LLC under Contract No. DE-AC02-98CH10886 with the U.S. Department of Energy. This manuscript has been authored in part by UT-Battelle, LLC, under Contract No. DE-AC05-00OR22725 with the U.S. DOE.

[1] I. Alekseev *et al.*, Configuration Manual, Polarized Proton Collider at RHIC, Rev. 2, Brookhaven National Laboratory,2006, https://www.bnl.gov/cad/accelerator/docs/pdf/rhicppcman.pdf.

[2] The Electron-Ion Collider, https://www.bnl.gov/eic/.

[3] W. MacKay *et al.*, Commissioning spin rotators in RHIC, in *Proceedings of the 20th Particle Accelerator Conference, PAC-2003, Portland, OR, 2003* (IEEE, New York, 2003), TPPB038, https://accelconf.web.cern.ch/p03/PAPERS/TPPB038.PDF.

[4] E. Willen, R. Gupta, A. Jain, E. Kelly, G. Morgan, J. Muratore, and R. Thomas, A helical magnet design for RHIC. in *Proceedings of the Particle Accelerator Conference, Vancouver, BC, Canada, 1997* (IEEE, New York, 1997), p. 3362, https://accelconf.web.cern.ch/pac97/papers/pdf/3P010.PDF.

[5] W. Fischer and M. Okamura, Parameterization and measurements of helical magnetic fields, in *Proceedings of the Particle Accelerator Conference, Vancouver, BC, Canada, 1997* (IEEE, New York, 1997), p. 3341, https://accelconf.web.cern.ch/pac97/papers/pdf/3P003.PDF.

[6] M. Okamura T. Tominaka, T. Kawaguchi, T. Katayama, A. Jain, J. Muratore, G. Morgan, and E. Willen, Half-length model of a Siberian snake magnet for RHIC, Nucl. Instrum. Methods Phys. Res., Sect. A **452**, 53 (2000).

[7] See, for instance, T. Tominaka *et al.*, Analytical field calculation of helical dipole magnets for RHIC, in *Proceedings of the Particle Accelerator Conference, Vancouver, BC, Canada, 1997* (IEEE, New York, 1997), https://accelconf.web.cern.ch/pac97/papers/pdf/6P018.PDF.

[8] M. Okamura, Three dimensional field analysis of helical snake magnets for RHIC, Report No. AGS/RHIC/SN 030, 1996, https://technotes.bnl.gov/PDF?publicationId=27333.

[9] A. Luccio *et al.*, Field map generated matrices for spin tracking, Wako, Japan, Report No. Riken-AF-NP-2351996; A. Luccio *et al.*, New capabilities of the spin tracking code SPINK, in *Proceedings of the 18th Particle Accelerator Conference, New York, 1999* (IEEE, New York, 1999), https://accelconf.web.cern.ch/p99/PAPERS/TUP44.PDF.

[10] Y. Dutheil, Spin dynamics modeling in the AGS based on a stepwise ray-tracing method, Ph.D. Dissertation, Brookhaven National Laboratory and J. Fourier University in Grenoble, https://www.osti.gov/biblio/1351801-spin-dynamics-modeling-ags-based-stepwise-ray-tracing-method.

[11] Y. Dutheil *et al.*, A model of the AGS based on stepwise ray-tracing through the measured field maps of the main magnets, in *Proceedings of the 3rd International Particle Accelerator Conference, New Orleans, LA, 2012* (IEEE, Piscataway, NJ, 2012), TUPPC101, https://accelconf.web.cern.ch/IPAC2012/papers/tuppc101.pdf.

[12] F. Méot *et al.*, Re-visiting RHIC snakes—OPERA fields, $\vec{n}_0$ dance, BNL Technical Note C-A/AP/590, (2017); https://technotes.bnl.gov/PDF?publicationId=42159.

[13] S. R. Mane, Yu. M. Shatunov, and K. Yokoya, Siberian snakes in high-energy accelerators, J. Phys. G **31**, R151 (2005).

[14] F. Méot, R. Gupta, H. Huang, V. Ranjbar, and W. Schmidke, Exploring a possible origin of an abnormal 10–15 degree spin tilt observed at RHIC polarimeters, in *Proceedings of 22nd International Spin Symposium, Urbana, IL* (University of Illinois and Indiana University, 2016), http://conferences.physics.illinois.edu/spin2016/proceedings.asp.

[15] F. Méot, H. Huang, and N. Tsoupas, On the image in RHIC of AGS $\vec{n}_0$, via the AtR, BNL Technical Note C-A/AP/502, 2013, https://technotes.bnl.gov/PDF?publicationId=37169.

[16] F. Méot *et al.*, RHIC blue snake blues, in *Proceedings of the 13th International Particle Accelerator Conference, Bangkok, Thailand*, https://ipac2022.vrws.de/papers/wepopt019.pdf; F. Méot *et al.*, RHIC Run 22, 9 o'clock, a snake in the blue. BNL Technical Note C-A/AP/661, 2022.

[17] V. Schoefer *et al.*, RHIC polarized proton operation in Run 22, *Proceedings of the 13th International Particle Accelerator Conference, Bangkok, Thailand*, https://ipac2022.vrws.de/papers/wepost031.pdf.

[18] H. Huang, J. Kewisch, C. Liu, A. Marusic, W. Meng, F. Méot, P. Oddo, V. Ptitsyn, V. Ranjbar, and T. Roser, High Spin-Flip Efficiency at 255 GeV for Polarized Protons in a Ring with Two Full Siberian Snakes, Phys. Rev. Lett. **120**, 264804 (2018).

[19] H. Huang, J. Kewisch, C. Liu, A. Marusic, W. Meng, F. Méot, P. Oddo, V. Ptitsyn, V. Ranjbar, T. Roser, and W. B. Schmidke, Measurement of the Spin Tune Using the Coherent Spin Motion of Polarized Protons in a Storage RingPhys. Rev. Lett. **122**, 204803 (2019).

[20] Yu. N. Filatov, A. M. Kondratenko, M. A. Kondratenko, V. V. Vorobyov, S. V. Vinogradov, E. D. Tsyplakov, A. D. Kovalenko, A. V. Butenko, Ya. S. Derbenev, and V. S. Morozov, Hadron polarization control at integer spin resonances in synchrotrons using a spin navigator, Phys. Rev. Accel. Beams **24**, 061001 (2021).

[21] V. Morozov *et al.*, Experimental verification of transparent spin mode in RHIC, in *Proceedings of the 10th International Particle Accelerator Conference, IPAC-2019, Melbourne, Australia, 2019* (JACoW, Geneva, Switzerland, 2019), https://accelconf.web.cern.ch/ipac2019/papers/wepgw122.pdf.

[22] H. Huang *et al.*, Simulation of transparent spin experiment in RHIC, in *Proceedings of the 4th North American Particle Accelerator Conference, NAPAC-2019, Lansing, MI* (JACoW, Geneva, Switzerland), https://accelconf.web.cern.ch/napac2019/papers/wepls11.pdf.

[23] F. Méot, Simulation tutorial: Spin transparency experiment at RHIC, BNL Technical Note C-A/AP/662, 2022.